TU Delft

Delft University of Technology

Damage mechanics model for correlating notch toughness in Charpy impact tests with fracture toughness in cracked static fracture tests

Wong, Wei Jun; Walters, Carey L.

DOI
10.1016/j.engfracmech.2025.111043

Publication date
2025

Document Version
Final published version

Published in
Engineering Fracture Mechanics

Citation (APA)
Wong, W. J., & Walters, C. L. (2025). Damage mechanics model for correlating notch toughness in Charpy impact tests with fracture toughness in cracked static fracture tests. *Engineering Fracture Mechanics*, *320*, Article 111043. https://doi.org/10.1016/j.engfracmech.2025.111043

Important note
To cite this publication, please use the final published version (if applicable).
Please check the document version above.

Copyright
Other than for strictly personal use, it is not permitted to download, forward or distribute the text or part of it, without the consent of the author(s) and/or copyright holder(s), unless the work is under an open content license such as Creative Commons.

Takedown policy
Please contact us and provide details if you believe this document breaches copyrights.
We will remove access to the work immediately and investigate your claim.

This work is downloaded from Delft University of Technology.
For technical reasons the number of authors shown on this cover page is limited to a maximum of 10.

Engineering Fracture Mechanics 320 (2025) 111043

Contents lists available at ScienceDirect

Engineering Fracture Mechanics

journal homepage: www.elsevier.com/locate/engfracmech

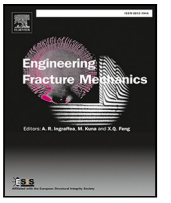

Damage mechanics model for correlating notch toughness in Charpy impact tests with fracture toughness in cracked static fracture tests

Wei Jun Wong *, Carey L. Walters

Department of Maritime and Transport Technology, Delft University of Technology, Mekelweg 2, Delft, 2628 CD, South Holland, The Netherlands

ARTICLE INFO

Keywords:
Failure strain
Flow plasticity
High-strength steel
Shear lips
Upper shelf

ABSTRACT

Empirically derived Charpy energy to fracture toughness (J-integral) correlations are often used to estimate the fracture toughness of steels from Charpy tests due to the higher testing costs and time associated with direct fracture toughness tests, but analytical insight into these correlations is lacking. Accounting for differences in the strain rates and stress states in these tests to simulate the correct response in both while keeping model complexity and calibration effort manageable presents an obstacle to a numerical approach for this problem. This paper hence establishes a modelling and calibration approach that could be used to contribute mechanics-based insight into the correlations between the Charpy energy, J-integral, yield-to-tensile strength ratio and tensile test fracture elongation. A phenomenological rate-dependent plasticity model coupled with damage and temperature effects is developed by implementing the strain-based modified Mohr–Coulomb damage-softening model with Johnson–Cook thermal softening in a thermodynamically consistent Cowper–Symonds viscoplasticity model. The validity of the modelling framework is shown by its ability to simultaneously model the tensile test, the Charpy V-notch test and the precracked single-edge notched bending test. This is demonstrated for two steels, AH36 and S690QL, capturing the force–displacement responses and the characteristic ductile fracture mechanism of slant fracture in all three tests. Accounting for thermal softening due to adiabatic heating proves to be important for the accurate simulation of ductile Charpy tests involving high impact energies. Capitalising on weak triaxiality dependence in the middle-to-high triaxiality ranges in the given materials and adopting a triaxiality-independent assumption is found to be effective for reducing the damage model complexity while maintaining its ability to simulate the mechanical response in key tests covering an important range of stress states. The importance of the role of the Lode angle in ductile fracture modelling in weakly triaxiality-dependent regimes is further substantiated. Key similarities in the fracture behaviour of the Charpy and single-edge notched bending tests are identified: they span a similar range of stress states over a large range of their response despite the initial notched versus cracked difference—an insight that could be used to reduce the calibration effort of damage mechanics models for these tests, assuming that the key differentiating factors of rate-dependence and adiabatic heating are correctly accounted for.

1. Introduction

Charpy V-notch impact tests and uniaxial tensile tests are relatively cheap and easy to perform in comparison with fracture toughness tests such as single-edge notched bending (SENB) tests which involve precracking. Although they do not provide a direct

* Corresponding author.
E-mail address: W.J.Wong@tudelft.nl (W.J. Wong).

https://doi.org/10.1016/j.engfracmech.2025.111043
Received 29 October 2024; Received in revised form 10 March 2025; Accepted 12 March 2025
Available online 22 March 2025
0013-7944/© 2025 The Authors. Published by Elsevier Ltd. This is an open access article under the CC BY-NC-ND license (http://creativecommons.org/licenses/by-nc-nd/4.0/).

Nomenclature

A

A	Fracture elongation over the proportional gauge length from pieced-together tensile test fragments
A_ε	Engineering strain at full fracture in tensile test
a_0	Measured initial crack length in SENB specimen
a_{0q}	Compliance-estimated initial crack length
a_n	Machined notch length in SENB specimen
Δa	Crack extension
Δa_{cp}	Crack extension from FEA crack-plane method
Δa_p	Measured final crack extension
Δa_{pq}	Compliance-estimated final crack extension
B	Specimen thickness
$\mathbb{C}$	Isotropic elastic stiffness tensor
C	Cowper–Symonds coefficient
C_1	Normalised MMC parameter relating to the strain in the MMC surface when $c_1 = 0; \eta = 2.5; \bar{\theta} = 0$
C_2	Normalised MMC parameter relating to the maximum strain in the MMC surface when $c_1 = 0$
C_3	Normalised MMC parameter relating to the minimum strain in the MMC surface when $c_1 = 0$
c	Specific heat capacity
c_1	First MMC strain surface parameter
c_2	Second MMC strain surface parameter
c_3	Third MMC strain surface parameter
C_v	Charpy V-notch energy
D	Damage indicator
D_c	Critical damage
$\mathcal{D}_p$	Internal work due to plastic deformation
E	Young's modulus
f	Yield function
h	Hardening modulus
i	Iteration
i_{max}	Maximum number of iterations for the return-mapping calculations
j	Increment
J	J-integral
J_{cp}	J-integral based on FEA crack-plane method
J_Q	Critical J based on the $0.2\,\mathrm{mm}$ crack extension offset
K	Strength coefficient for the hardening power law
K_J	Stress intensity factor converted from J
L	Single-edge notched bending specimen length
L_0	Gauge length of tensile specimen
L_c	Parallel length of tensile specimen
l_c	Characteristic element length
m	Damage softening exponent
m_x	Thermal softening exponent
N	Notch-mouth/knife-edge opening
n	Strain hardening exponent
$\boldsymbol{n}$	Gradient of the yield surface
$\boldsymbol{P}$	Pseudo-elastic material stiffness matrix
q	Cowper–Symonds exponent
R	Rate-dependence factor
S	Single-edge notched bending specimen span
s	Viscosity parameter
Δt	Time increment
T	Interpolation parameter

W	Specimen width
w	SENB machined notch width
X	Thermal softening factor
Z	Parameter for the grouped effect of the MMC c_1 terms when $\eta = 2.5$; $\bar{\theta} = 0$
B	
α	Plastic coefficient
β	Softening coefficient
ε	Engineering strain
ε_0	Swift offset strain
ε_f	Ductile damage initiation strain
ε_p	Equivalent plastic strain
$\dot{\varepsilon}$	Uniaxial strain rate
$\dot{\varepsilon}_p$	Equivalent plastic strain rate
$\dot{\varepsilon}_{p0}$	Equivalent plastic strain rate offset parameter
$\dot{\varepsilon}_{p,uni}$	Quasi-static-uniaxial-testing equivalent plastic strain rate parameter
$\ddot{\varepsilon}_p$	Rate of change of the plastic strain rate
ε_{sh}	Total engineering strain corresponding to the end of the yield plateau
$\varepsilon_{sh,p}$	Equivalent plastic strain corresponding to the end of the yield plateau
ε_u	Uniform elongation, i.e. the engineering strain at the onset of necking
$\varepsilon_{u,p}$	Equivalent plastic strain corresponding to the occurrence of necking instability
$\dot{\boldsymbol{\varepsilon}}_{\boldsymbol{vp}}$	Viscoplastic strain rate tensor
$\Delta\boldsymbol{\varepsilon}_{\boldsymbol{vp}}$	Viscoplastic strain increment tensor
η	Stress triaxiality
Θ	Temperature
Θ_m	Melting temperature
Θ_r	Room temperature
$\bar{\theta}$	Normalised Lode angle
$\dot{\lambda}$	Plastic multiplier as a rate
$\Delta\lambda$	Plastic multiplier as an increment
μ_D	Tolerance for $D = D_c$ when i_{max} is reached
μ_f	Tolerance for $f = 0$
ν	Poisson's ratio
ρ	Density
σ	Flow stress taking into account plastic strain hardening, rate dependence and damage due to softening
$\bar{\sigma}$	Quasi-static undamaged stress due to plastic strain hardening only
σ_v	von Mises equivalent stress
σ_u	Ultimate tensile stress from uniaxial tensile test
σ_y	Yield stress from uniaxial tensile test
$\boldsymbol{\sigma}$	Cauchy stress tensor
χ	Taylor–Quinney energy coefficient
C	
CMOD	Crack-mouth opening displacement
CTOD	Crack-tip opening displacement
DWTT	Drop-weight tear test
FEA	Finite-element analysis
MMC	Modified Mohr–Coulomb
SENB	Single-edge notched bending

measure of the fracture toughness, the Charpy test gives a notch (uncracked) toughness, and the tensile test gives information about the strain hardening and ductility. These tests are hence often used as part of the product certification and structural design process in the construction industry to assess fracture toughness indirectly, in addition to their usual purpose of measuring strength (tensile test) and the ductile-to-brittle transition temperature (Charpy test). This use of the uncracked properties to estimate cracked

properties appears in two application contexts: the assessment of the acceptability of flaws for fitness-of-service [1] and the design for the ultimate ductile fracture strength at areas where cracks due to fatigue or manufacturing defects might be expected to induce stress concentrations and high local plastic straining [2,3].

In the assessment of the acceptability of flaws, upper-shelf C_v values are sometimes used to estimate the upper-shelf fracture toughness value in terms of J or an equivalent stress intensity factor K_J converted from J [1,4] based on empirical correlations when direct fracture toughness data is not available. The material's fracture toughness is then used for comparison with the applied stress intensity for the flaw to assess its safety.

In the ultimate strength design for ductile fracture in areas where fatigue or manufacturing processes might cause cracks or crack-like defects [2], the combination of limits on the Charpy impact energy C_v, the fracture elongation A and the yield-to-tensile strength ratio σ_y/σ_u is often implicitly adopted as a substitute upper-shelf toughness criterion [5,6]. In this context, the minimum C_v functions as a provision for the avoidance of brittle behaviour, and the minimum A and maximum σ_y/σ_u act as ductility requirements that, when complemented with strength based design, are assumed to indirectly account for the upper-shelf toughness [7]. However, this has been shown to be inadequate in certain situations, and the mechanical basis for these assumptions are lacking [5,6,8]. The most recent developments have therefore seen minimum upper-shelf C_v values (e.g. 100 J [3,5]) being used for some design situations as an improved but nonetheless indirect upper-shelf fracture toughness requirement. This further accentuates the need for a better understanding of $C_v - J$ correlations.

Due to the practicality and usefulness of these upper-shelf $C_v - J$ correlations, various studies have been performed to improve their accuracy [4,9–14]. Some studies also estimated fracture toughness using force–displacement data from the instrumented Charpy test [15,16], instead of the total impact energy alone. However, the correlations mentioned above have been developed using predominantly empirical methods, and although the existing work on the modelling of Charpy test and precracked fracture tests using phenomenological and micromechanical material models in the literature is extensive [17–21], a few complexities need to be overcome to relate C_v and J using such numerical models.

First, the existing studies on the numerical modelling of Charpy and SENB tests are separate and based on various models of varying complexity, while correlating C_v and J necessitates a single model that has been proven to reliably and accurately simulate the behaviour in both the Charpy and SENB tests. The differences between the strain rates and the stress states experienced in these tests present notable challenges. High strain rates have an effect of increasing the plastic flow stress [22]. A Charpy test experiences plastic strain rates of up to the order of $10^4\ s^{-1}$ [23,24], while the SENB test is a quasi-static test with strain rates around the order of $10^{-2}\ s^{-1}$. At the same time, the stress states occurring at the notch tip of the Charpy specimen and the crack tip of the SENB specimen are markedly different, and the onset of fracture is known to depend on the stress state. However, a full calibration of the stress-state dependent fracture model to all possible stress states for a single material requires extensive experimentation [25]. A model that is intended for relating C_v and J for the large variety of materials and the relatively limited material characterisation data expected in the above-mentioned engineering contexts requires relative ease of calibration without losing the capability to capture the ductile and rate-dependent aspects sufficiently accurately.

Second, ductile fracture often involves slant fracture, which is fracture that occurs in a direction that is slanted with respect to the direction of the maximum principal stress. Being able to simulate slant fracture occurrence is important because it is a characteristic feature of ductile fracture behaviour, and increased slant fracture occurrence has been correlated with properties such as reduced strain hardenability [26], increased loading rate [27], and greater specimen thickness [26]. While slant fracture behaviour has been successfully captured in simulations of uncracked quasi-static [28–30], cracked quasi-static [19,30,31] and sharply notched[1] dynamic [32,33] tests, simulating an uncracked, dynamic and rate-dependent Charpy test that accounts for the ductile slant fracture behaviour proves to be a challenge[2] [17,18,37], let alone accounting for it in both the Charpy and the static fracture toughness test using one material model.

Therefore, a model that emphasises the balance between model simplicity, generalisability and capability to simulate complex behaviour in both the Charpy and SENB test is developed and presented in this paper. A thermodynamically consistent phenomenological rate-dependent damage-softening material model is used in finite-element calculations of fracture toughness (from single-edge notched bending specimens), notch toughness (from Charpy specimens) and ductility (from uniaxial tensile specimens). The model formulation is given in Section 2. Sections 4 to 6 describe the calibration of the model parameters to experiments on an S690QL [38] steel and an AH36 [39] steel. The validity of the modelling framework is shown by its ability to simultaneously model the 3 mechanical tests involving different stress states, strain rates and geometries (cracked and uncracked) with the same input parameter values describing the given material, capturing the measured mechanical properties, the load-deformation response and the characteristically ductile slant fracture surfaces with reasonable accuracy. Attention is given to the effects of the material parameters on the resulting mechanical properties.

[1] Though not precracked by fatigue, dynamic drop-weight tear tests such as those performed in [32,33] involve a sharp chiselled notch which has a much smaller radius, between 0.013 and 0.025 mm [34], than in Charpy tests, which have a notch radius of 0.25 mm [35].

[2] An earlier version of the present model has been shown to capture slant fracture in Charpy-test simulations in a recent conference paper [36] on the effect of strain hardening and of Lode dependence of the fracture strain on slant fracture in Charpy test simulations.

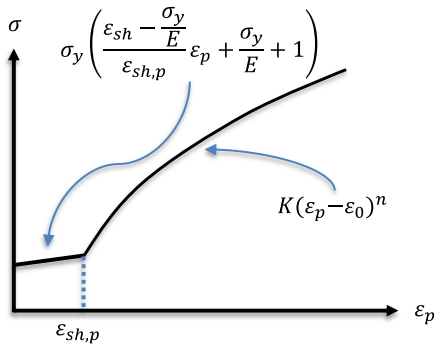

Fig. 1. Swift-type [42] power-law true stress–strain curve with a yield plateau.

2. Consistency model for viscoplasticity with damage softening and thermal softening

In this work, the elasto-viscoplastic consistency model [40] with an associated flow rule is coupled with damage softening [28] and thermal softening [41] acting on the plastic hardening function. Von Mises yielding is assumed such that the yield function is expressed as:

$$f = \sigma_v - \bar{\sigma} R \beta X \tag{1}$$

where σ_v is the von Mises equivalent stress; $\bar{\sigma}$ is the plastic strain-hardening stress (Section 2.1); R is the rate-dependence factor (Section 2.2); β is the softening coefficient (Section 2.3); X is the thermal softening factor (Section 2.4); and $\sigma = \bar{\sigma} R \beta X$ is the flow stress. Incremental stresses due to these effects coupled in Eq. (1) are calculated using a return mapping solution ensuring thermodynamical consistency (Section 2.5).

2.1. Plastic hardening model

A quasi-static undamaged true plastic stress–strain relation (Fig. 1) that features a yield plateau and a Swift [42] hardening curve (Eqs. (2) and (3)) is used:

$$\bar{\sigma} = \begin{cases} \sigma_y \left(\dfrac{\varepsilon_{sh} - \frac{\sigma_y}{E}}{\varepsilon_{sh,p}} \varepsilon_p + \frac{\sigma_y}{E} + 1 \right) & 0 < \varepsilon_p < \varepsilon_{sh,p} \\ K(\varepsilon_p - \varepsilon_0)^n & \varepsilon_p \geq \varepsilon_{sh,p} \end{cases} \tag{2}$$

$$\varepsilon_{sh,p} = \ln(1+\varepsilon_{sh}) - \ln\left(1 + \frac{\sigma_y}{E}\right) \tag{3}$$

where $\bar{\sigma}$ is the plastic strain hardening stress; ε_p is the true equivalent plastic strain; ε_{sh} and $\varepsilon_{sh,p}$ are respectively the total engineering strain and the true equivalent plastic strain corresponding to the end of the yield plateau; K is the strength coefficient; n is the strain hardening exponent; and ε_0 is the Swift [42] offset parameter. The slight hardening in the yield plateau in Eq. (2) arises from converting a flat plateau expressed in terms of engineering stress into one that is expressed in terms of true stress. A convention with a negative symbol in $K(\varepsilon_p - \varepsilon_0)^n$ is used so that the material parameter value ε_0 is typically specified in the positive rather than negative range, since a Swift-type curve (in Eq. (2)) that is translated towards positive ε_p values is seen to apply for the materials and assumptions considered in this work.

Given the Young's modulus E, yield strength σ_y, ultimate strength σ_u, yield plateau length ε_{sh} and the uniform (necking) elongation ε_u, the parameters n, K and ε_0 of the plastic hardening model can be estimated using theoretical knowledge about the strain hardening's relation to the ultimate strength σ_u induced by necking. This is done by assuming that σ_u satisfies the Considère [43] criterion for necking, which results in Eqs. (4) and (5).

$$n = \varepsilon_{u,p} - \varepsilon_0 \tag{4}$$

$$K\left(\varepsilon_{u,p} - \varepsilon_0\right)^n = \sigma_u\left(1 + \varepsilon_u\right) \tag{5}$$

where $\varepsilon_{u,p}$ is the true plastic strain corresponding to the occurrence of necking instability and the ultimate tensile stress, which is related to ε_u by:

$$\varepsilon_{u,p} = \ln\left(1 + \varepsilon_u\right) - \ln\left(1 + \frac{\sigma_u}{E}\right) \tag{6}$$

In addition, considering that the power curve intersects with the yield plateau at a true plastic strain $\varepsilon_p = \varepsilon_{sh,p}$ results in Eq. (7):

$$K\left(\varepsilon_{sh,p} - \varepsilon_0\right)^n = \sigma_y(1 + \varepsilon_{sh}) \tag{7}$$

Combining Eqs. (3) to (7) enables K, n and ε_0 to be solved and the true stress–strain curve to be approximated, given σ_y, σ_u, E, ε_{sh} and ε_u. It will be seen in Section 4 below that these assumptions give good predictions of the engineering stress–strain response until necking, using only the experimental σ_y, σ_u, E, ε_{sh} and ε_u as input. This semi-analytical approach to the description of the true stress–strain curve is valuable for engineering applications, because in typical situations during the testing for material certification for structural steels, the entire stress–strain history is not available. However, the σ_y and σ_u are recorded in the material test certificates, while empirical relations for ε_{sh} and ε_u obtained from large databases for structural steels exist [44,45].

2.2. Rate-dependence model

To take the effect of the strain rate on the plastic flow stress into account, the plastic stress–strain curve is scaled based on the Cowper–Symonds model [22]. The original formulation of the Cowper–Symonds [22] model is shown in Eq. (8):

$$R = 1 + \left(\frac{\dot{\varepsilon}}{C}\right)^{\frac{1}{q}} \tag{8}$$

where R is the rate-dependence factor by which the static flow stress is to be multiplied to give the rate-dependent yield stress; $\dot{\varepsilon}$ is the uniaxial strain rate; C is the Cowper–Symonds coefficient; and q is the Cowper–Symonds exponent.

To enable this to be applied to the viscoplastic consistency model presently used, two modifications are implemented. First, the strain-rate effect given by R, which is determined experimentally in the literature with respect to the uniaxial strain rate $\dot{\varepsilon}$, is assumed to act equivalently with respect to the equivalent plastic strain rate $\dot{\varepsilon}_p$. This is in accordance with the understanding that, for incompressible materials subject to uniaxial tension, $\dot{\varepsilon}_p$ is by definition equal to $\dot{\varepsilon}$ until necking. Second, the parameter $\dot{\varepsilon}_{p0}$ is introduced to enable the translation of the R versus $\dot{\varepsilon}_p$ relation with respect to the $\dot{\varepsilon}_p$ axis by $-\dot{\varepsilon}_{p0}$, so that the gradient of R with respect to $\dot{\varepsilon}_p$ is finite for $\dot{\varepsilon}_p = 0\,\mathrm{s}^{-1}$, since this is required for the return mapping calculations (Section 2.5) to converge, and this gradient in the original formulation is infinite. Additionally, $R = 1$ is made to coincide with $\dot{\varepsilon}_p = \dot{\varepsilon}_{p,uni}$, the equivalent plastic strain rate corresponding to uniaxial testing through the use of a translation in the R-axis.

This results in the equation for R implemented in the present model:

$$R = 1 - \left(\frac{\dot{\varepsilon}_{p,uni} + \dot{\varepsilon}_{p0}}{C}\right)^{\frac{1}{q}} + \left(\frac{\dot{\varepsilon}_p + \dot{\varepsilon}_{p0}}{C}\right)^{\frac{1}{q}} \tag{9}$$

The quasi-static-uniaxial-testing equivalent plastic strain rate parameter $\dot{\varepsilon}_{p,uni}$ is here taken to be $0.000\,25\,\mathrm{s}^{-1}$ according to the ISO 6892-1 tensile testing standard [46], and the same value is assumed for the small translation $\dot{\varepsilon}_0 = \dot{\varepsilon}_{p,uni}$. Least-squares fitting to existing experimental data was performed to obtain the Cowper–Symonds parameters for structural steels with nominal strengths in the range of 345 to 355 MPa [47–53] and 690 MPa [54–57] separately, as shown in Fig. 2, for use in the simulations of the tested AH36 and S690QL steels. The data from Dong et al. [58] was not included in the fit, due to its nature as an outlier, in which all except two points from this source plotted below the mutually overlapping data cloud formed by the other sources.

In addition to accounting for the high strain rate occurring in Charpy tests, the rate dependence introduces viscosity, which has the important role of helping to eliminate the mesh sensitivity (non-convergence with mesh refinement) [40,59] faced by local approaches to material softening such as the classic MMC damage-softening model [28].

2.3. Damage model

To describe the initiation of damage softening, the strain formulation of the modified Mohr–Coulomb (MMC) [60] fracture surface is used:

$$\varepsilon_f = \left\{\frac{K}{c_2}\left[c_3 + \frac{\sqrt{3}}{2-\sqrt{3}}(1-c_3)\left(\sec\frac{\bar{\theta}\pi}{6} - 1\right)\right]\left[\sqrt{\frac{1+{c_1}^2}{3}}\cos\frac{\bar{\theta}\pi}{6} + c_1\left(\eta + \frac{1}{3}\sin\frac{\bar{\theta}\pi}{6}\right)\right]\right\}^{-\frac{1}{n}} \tag{10}$$

where ε_f is the damage initiation strain; η is the stress triaxiality; $\bar{\theta}$ is the normalised Lode-angle [61]; and c_1, c_2 and c_3 are the MMC model parameters. K and c_2 have the units of stress, while n, c_1 and c_3 are dimensionless.

The sum of the incremental equivalent plastic strains relative to the instantaneous ε_f is used to quantify the amount of damage, as given by the damage indicator D:

$$D = \int_0^{\varepsilon_p} \frac{1}{\varepsilon_f}\, d\varepsilon_p \tag{11}$$

Material softening starts when enough plastic straining has occurred such that $D = 1$, and complete degradation (corresponding to finite element deletion) occurs when D reaches the critical damage value D_c, as described by Eq. (12) [28]:

$$\beta = \begin{cases} 1 & D \le 1 \\ \left(\dfrac{D_c - D}{D_c - 1}\right)^m & 1 < D < D_c \\ 0 & D = D_c \end{cases} \tag{12}$$

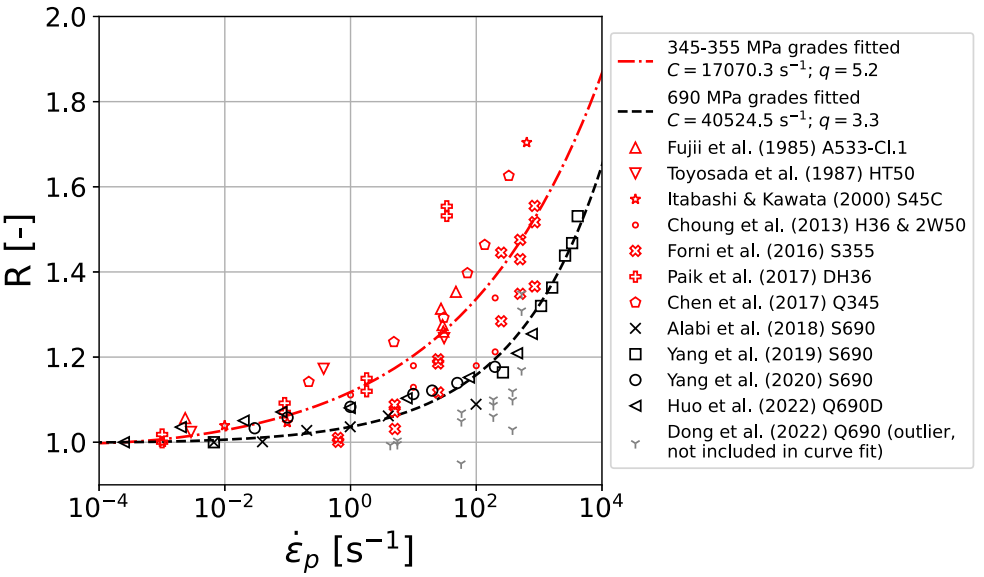

Fig. 2. Least-squares fit of R and experimental data from the literature [47–58].

where β is the softening parameter in the yield function (Eq. (1)), and m is the softening exponent.

It is worth noting that the use of Eq. (12) implies that the MMC locus (Eq. (10)) defines the damage initiation strains instead of the fracture initiation strains as assumed in the original uncoupled version of the MMC model [60]. This slight modification facilitates the coupling of softening effects to the MMC model based on stress-state-dependent damage softening initiation criterion and has been effectively applied by several others for the modelling of softening behaviour in steel [28,62,63] and aluminium [64].

It should also be noted that here, the formulation of the MMC fracture strain surface is accepted as is, but for simplicity, the associated Lode-dependent Bai–Wierzbicki hardening rule [60,61] used to derive the MMC strain surface is not adopted. Although a different strain hardening rule (Eq. (2)) is used here, the c_3 originating from the Bai–Wierzbicki hardening rule is kept as a parameter in the failure strain surface for its use in controlling the failure strain's Lode-dependence. As a result of this, the present approach uses a strain-based damage initiation criterion instead of the stress-based damage initiation criterion on which the MMC model was originally established. The stress at the occurrence of the damage initiation strain does not necessarily coincide with the stress given by the original MMC stress envelope [60]. The MMC failure strain surface is assumed to be in itself suitable for phenomenologically describing the fracture strains regardless of the MMC stresses. This widely used phenomenological, strain-based take of the MMC fracture model has been successful in describing ductile fracture behaviour in both precracked [62,63] and initially uncracked [28,64,65] geometries, performing well over a wide range of stress triaxialities and Lode angles, while involving only 3 damage initiation parameters.

The parameter c_1 determines the triaxiality dependence of the damage initiation strain. Notably, $c_1 = 0$ corresponds to the limiting case of the maximum shear stress fracture criterion which with von Mises yielding traditionally reduces to a single-parameter (c_2) fracture model. Furthermore, the parameters c_2 and c_3 can be rewritten in a normalised form that relates directly to the maximum and minimum strains on the $c_1 = 0$ fracture strain locus, for ease of comparison during strain-based calibration, as given by Eqs. (13) and (14):

$$C_2 = \left(\frac{2c_2}{K}\right)^{\frac{1}{n}} \tag{13}$$

$$C_3 = \left(\frac{\sqrt{3}c_2}{Kc_3}\right)^{\frac{1}{n}} \tag{14}$$

C_2 is given by the expression for ε_f when $c_1 = 0$ and $\bar{\theta} = \pm 1$; and C_3 is given by the expression for ε_f when $c_1 = \bar{\theta} = 0$. The effect of this is that the maximum strain in the fracture strain surface is always equal to C_2, and the minimum strain of the fracture strain surface is always equal to C_3, regardless of the values of K and n.

C_1, a normalised form of c_1, is introduced as shown in Eqs. (15) and (16), for the ease of strain-based comparison when considering the triaxiality dependence of the fracture strain locus. $C_1 = C_3$ corresponds to the triaxiality-independent $c_1 = 0$ condition, and changing C_1 introduces triaxiality dependence by adjusting the triaxiality-independent fracture strain locus to pass through $\varepsilon_f = C_1$ at $\bar{\theta} = 0$ and $\eta = 2.5$, which is the perfectly plastic, plane-strain solution for the stress state in front of the crack tip [66].

$$C_1 = \left(\frac{c_2}{c_3 KZ}\right)^{\frac{1}{n}} \tag{15}$$

where Z is given by:

$$Z = \sqrt{\frac{1 + {c_1}^2}{3}} + 2.5c_1 \tag{16}$$

Substituting Eqs. (13) to (16) into Eq. (10) gives an expression for ε_f in terms of the normalised parameters C_1, C_2 and C_3, instead of c_1, c_2 and c_3:

$$\varepsilon_f = C_2 \left(\left(\sqrt{3} \left(\frac{C_2}{C_3} \right)^n - \frac{3 \cdot 5^2 \cdot 37 \cdot 1311338992127}{2^{48}} \left(\sec \frac{\bar{\theta}\pi}{6} - 1 \right) \left(\frac{\sqrt{3}}{2} \left(\frac{C_2}{C_3} \right)^n - 1 \right) \right) \cdot \left(\cos \frac{\bar{\theta}\pi}{6} \sqrt{\frac{{c_{11}}^2 + 1}{3}} + \frac{c_{11}}{3} \left(\eta + \sin \frac{\bar{\theta}\pi}{6} \right) \right) \right)^{-\frac{1}{n}} \tag{17}$$

where c_{11} is given by:

$$c_{11} = \frac{2}{71} \left(-\sqrt{4 \left(\frac{C_3}{C_1} \right)^{2n} + 71} + 5\sqrt{3} \left(\frac{C_3}{C_1} \right)^n \right) \tag{18}$$

A negative triaxiality cut-off value of $\eta = -1/3$ [67] for the damage initiation criterion is introduced by additionally increasing the ε_f, given by (Eq. (10)), quickly but continuously as η drops below $-1/3$. For high triaxialities exceeding 3.5, the ε_f is kept at a constant level determined by its value at $\eta = 3.5$, which typically only comes into effect when an element has $D > 1$ and is near deletion. The continuous nature of the addition to ε_f below the cut-off triaxiality and the constant ε_f for high η ensure that ε_f does not have extremely large or small values in those η ranges, which would cause convergence errors.

2.4. Thermal softening model

The dynamic Charpy test occurs at time scales that can be approximated as adiabatic [23]. Studies considering the effect of adiabatic heating on the Charpy impact test by Tanguy et al. [68] and Seo et al. [69] using temperature-dependent material models have shown that the thermal softening caused by adiabatic heating in the Charpy tests should not be neglected. Here, a thermal softening factor based on the Johnson–Cook [41] plasticity model is adopted in the yield function (Eq. (1)) for the Charpy simulation, as given in Eq. (19):

$$X = 1 - \left(\frac{\Theta - \Theta_r}{\Theta_m - \Theta_r} \right)^{m_x} \tag{19}$$

where Θ is the temperature, Θ_m is the melting temperature, Θ_r is the room temperature, and m_x is the thermal softening exponent.

The rate of change of temperature at each material point at each increment is calculated from Eq. (20):

$$\dot{\Theta} = \frac{\chi \dot{\mathcal{D}}_p}{c} \tag{20}$$

where χ is the Taylor–Quinney [70] energy coefficient, c is the specific heat capacity of the material, and $\dot{\mathcal{D}}_p$ is the rate of internal work done attributed to plastic deformation as given by Eq. (21) [71]:

$$\dot{\mathcal{D}}_p = \frac{\boldsymbol{\sigma} : \dot{\boldsymbol{\varepsilon}}_{vp}}{\rho} \tag{21}$$

where $\boldsymbol{\sigma}$ is the Cauchy stress tensor, $\dot{\boldsymbol{\varepsilon}}_{vp}$ is the viscoplastic strain rate tensor, and ρ is the density of the material.

The proportion χ of the internal work due to plastic deformation $\mathcal{D}_p$ that is converted to heat is assumed to be 0.9, as proposed by Meyers [72], where the remaining latent part of the work is associated with defects and changes in the physical properties of the crystalline material [70,72] (e.g. dislocation pile-ups). Values of Θ_m, Θ_r, m_x, c found in the literature for low carbon steels with yield strength and chemical composition similar to the present steels are adopted here. For the AH36 steel, the parameters for the similarly graded low-carbon, low-alloy X52 [73] pipeline steel reported by Seo et al. [69] and Liakat and Khonsari [74] are used, being $\Theta_m = 1500\,°\text{C}$, $\Theta_r = 25\,°\text{C}$, $m_x = 0.8$ and $c = 480\,\text{J/kg/°C}$. For the S690QL steel, the parameters for Weldox 700 E steel (which fulfils the S690QL standard [38]) reported by Dey et al. [75] are used, being $\Theta_m = 1527\,°\text{C}$, $\Theta_r = 20\,°\text{C}$, $m_x = 1.071$ and $c = 452\,\text{J/kg/°C}$.

Thermal conductivity is neglected due to the short time frame and the high plastic strain rate, and thermal expansion is neglected since the adiabatic heating is primarily concentrated in areas with large plastic strains [68]. The quasi-static tensile and SENB tests are modelled as isothermal and without any temperature dependence, such that X is constant and equal to 1.

2.5. Stress-update algorithm and return mapping for coupled thermal- and damage-softening viscoplasticity model

The plasticity calculations involve solving for the stress increment which satisfies the consistency condition $\dot{f} = 0$, i.e. that when yielding, the stress state stays on the yield surface, which evolves according to the assumed plastic-hardening (Section 2.1),

damage-softening (Section 2.3), and rate-dependent (Section 2.2) behaviour. The yield function f (Eq. (1)) can be expressed in terms of its variables as:

$$f(\boldsymbol{\sigma}, \varepsilon_p, \dot{\varepsilon}_p) = \sigma_v(\boldsymbol{\sigma}) - \bar{\sigma}(\varepsilon_p) R(\dot{\varepsilon}_p) \beta(D(\varepsilon_p)) X(\Theta(\varepsilon_p)) \tag{22}$$

The consistency condition $\dot{f} = 0$ according to the consistency model of Wang et al. [40] is then given by:

$$\dot{f}(\boldsymbol{\sigma}, \varepsilon_p, \dot{\varepsilon}_p) = \frac{\partial f}{\partial \boldsymbol{\sigma}} \dot{\boldsymbol{\sigma}} + \frac{\partial f}{\partial \varepsilon_p} \dot{\varepsilon}_p + \frac{\partial f}{\partial \dot{\varepsilon}_p} \ddot{\varepsilon}_p = 0 \tag{23}$$

To solve this for the present formulation, the iterative implicit Euler-backward stress-update algorithm by Wang et al. [40] for their viscoplastic model is adapted such that it is coupled with the damage-softening of Li and Wierzbicki [28] (Section 2.3) and the Johnson–Cook [41] thermal softening model (Section 2.4) and such that the rate-dependent effect can be defined according to the Cowper–Symonds model [22] (Section 2.2).

First, the associated flow rule [76] is assumed:

$$\dot{\boldsymbol{\varepsilon}}_{\boldsymbol{vp}} = \dot{\lambda} \boldsymbol{n} \tag{24}$$

where $\dot{\boldsymbol{\varepsilon}}_{\boldsymbol{vp}}$ is the viscoplastic strain rate tensor; $\boldsymbol{n} = \dfrac{\partial f}{\partial \boldsymbol{\sigma}}$ is the gradient of the yield surface; and $\dot{\lambda}$ is the plastic strain rate multiplier.

By substituting the associated flow rule (Eq. (24)) into the definition of the equivalent plastic strain rate, $\dot{\varepsilon}_p$ can be expressed as shown in Eq. (25):

$$\dot{\varepsilon}_p = \dot{\lambda} \alpha = \dot{\lambda} \tag{25}$$

where $\alpha = \sqrt{\frac{2}{3} \boldsymbol{n} \cdot \boldsymbol{n}}$, termed the plastic coefficient, is always equal to 1 in the present study, due to the assumption of von Mises yielding (Eq. (22)). Furthermore, substituting the associated flow rule with von Mises yielding (Eqs. (24) and (25)) into Eq. (21) allows $\dot{D}_p$ to be expressed in terms of equivalent stress and equivalent strain (Eq. (26)). This makes the change in temperature a simple function of the change in equivalent plastic strain, such that Θ does not need to be solved as an extra independent variable in iterative solution of the yield and consistency functions (Eqs. (22) and (23)).

$$\dot{D}_p = \frac{\sigma_v \dot{\varepsilon}_p}{\rho} \tag{26}$$

Substituting Eq. (25) into Eq. (23), it becomes convenient to define a hardening modulus h and a viscosity parameter s [40] for the iterative solution of Eq. (23), such that:

$$\dot{f}(\boldsymbol{\sigma}, \varepsilon_p, \dot{\varepsilon}_p) = \boldsymbol{n} \dot{\boldsymbol{\sigma}} - h \dot{\lambda} - s \ddot{\lambda} \tag{27}$$

where h and s can then be expressed in terms of the parameters of the Li and Wierzbicki [28] damage-softening model, the Cowper–Symonds [22] rate-dependence model and the Johnson–Cook [41] thermal softening model:

$$h = -\frac{\partial f}{\partial \varepsilon_p} \frac{\dot{\varepsilon}_p}{\dot{\lambda}} = R \left(\frac{\partial \beta}{\partial \varepsilon_p} \bar{\sigma} X + \frac{\partial \bar{\sigma}}{\partial \varepsilon_p} \beta X + \frac{\partial X}{\partial \varepsilon_p} \bar{\sigma} \beta \right) \tag{28}$$

$$s = -\frac{\partial f}{\partial \dot{\varepsilon}_p} \frac{\ddot{\varepsilon}_p}{\ddot{\lambda}} = \frac{\partial R}{\partial \dot{\varepsilon}_p} \beta \bar{\sigma} X \tag{29}$$

From Eqs. (2), (9), (11), (19), (20) and (26), $\dfrac{\partial \beta}{\partial \varepsilon_p}$, $\dfrac{\partial \bar{\sigma}}{\partial \varepsilon_p}$, $\dfrac{\partial X}{\partial \varepsilon_p}$ and $\dfrac{\partial R}{\partial \dot{\varepsilon}_p}$ can be expressed as shown in Eqs. (30) to (33).

$$\frac{\partial \beta}{\partial \varepsilon_p} = \begin{cases} 0 & D \le 1 \\ -\frac{m\beta}{\varepsilon_f (D_c - D)} & 1 < D < D_c \end{cases} \tag{30}$$

$$\frac{\partial \bar{\sigma}}{\partial \varepsilon_p} = \begin{cases} \sigma_y \frac{\varepsilon_{sh} - \frac{\sigma_y}{E}}{\varepsilon_{sh,p}} & 0 < \varepsilon_p < \varepsilon_{sh,p} \\ K n {\varepsilon_p}^{n-1} & \varepsilon_p > \varepsilon_{sh,p} \end{cases} \tag{31}$$

$$\frac{\partial X}{\partial \varepsilon_p} = -\frac{m_x \chi \sigma_v}{\rho c (\Theta_m - \Theta_r)} \left(\frac{\Theta - \Theta_r}{\Theta_m - \Theta_r} \right)^{m_x - 1} \tag{32}$$

$$\frac{\partial R}{\partial \dot{\varepsilon}_p} = \frac{1}{q(\dot{\varepsilon}_p + \dot{\varepsilon}_{p0})} \left(\frac{\dot{\varepsilon}_p + \dot{\varepsilon}_{p0}}{C} \right)^{\frac{1}{q}} \tag{33}$$

The expanded algorithm for the iterative solution of Eq. (23) to find the incremental plastic strains and updated stresses in each plastic FEA increment, implemented as a VUMAT subroutine in Abaqus Explicit [77], is shown in the Appendix. The description above highlights only the model details specific to the present formulation. Details on the other aspects of the consistency model and algorithm can be found in [40,78]. It is worth noting that this elasto-viscoplastic consistency model is, as its name suggests, thermodynamically consistent, because the consistency condition (Eq. (23)) and the Kuhn–Tucker [79] relations are satisfied in the stress-update calculations (Appendix).

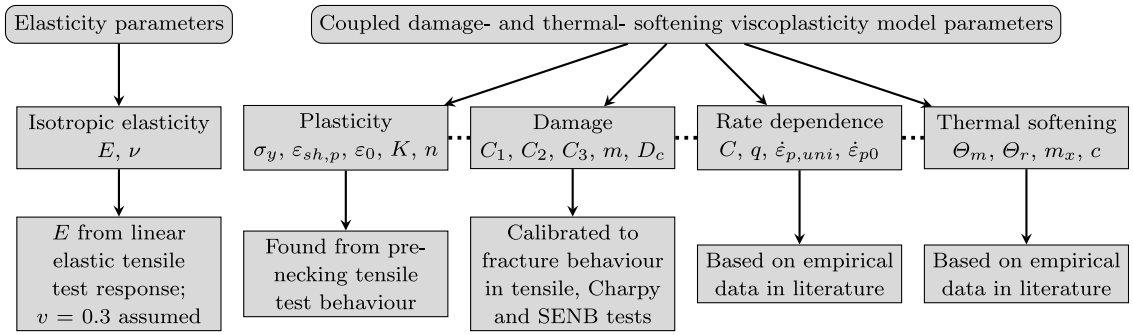

Fig. 3. Model parameters.

3. Model calibration to experiments

The calibration of ductile damage models using conventional methods requires considerable experimental and numerical modelling effort. Since the fracture behaviour depends on the stress state, the traditional approach to calibrating damage models involves a series of experiments on specimens with geometries that induce specific stress states in order to determine the stress-state-dependent fracture locus experimentally. This is often achieved by using variations of the tension, butterfly, notched or grooved specimens. Digital image correlation or reverse-engineering with numerical models, or both, are often required to determine obtain the fracture strains from these tests [25,80].

Recent work in the literature has achieved some success in simplifying this calibration process for certain cases, such as the SENB-based calibration procedure proposed by Coppejans and Walters [81] and the uniaxial-tensile-test-based procedure proposed by Xin and Veljkovic [82]. In a similar vein, this work reduces the experimental effort by calibrating the model parameters using the mechanical (force–displacement and energy) response of the uniaxial tensile test, the instrumented Charpy test and the single-edge notched bending test, while ensuring that the ductile fracture mechanism observed in the slant crack propagation behaviour is captured. A considerable range of triaxialities is involved, despite the relatively low number of tests (1/3 pre-necking in the tensile test; $\sim$ 1.7 before crack growth in the Charpy; and $\sim$ 2.2 before crack growth in the SENB). Since tensile tests and instrumented Charpy tests are widely used and easily performed, the only significant effort arises in the single-edge notched bending test.

Fig. 3 summarises the material parameters of the present model and the associated calibration processes. The Young's modulus E is obtained from the linear-elastic stiffness of the uniaxial tensile test, and the Poisson's ratio ν is assumed to be 0.3. The plasticity parameters σ_y, $\varepsilon_{sh,p}$, K, n and ε_0 are found from the pre-necking tensile behaviour as described in Section 2.1. The rate dependence parameters C and q are estimated using a least-squares fit of the Cowper–Symonds [22] curve to empirical data in the literature, while the other rate dependence parameters $\dot{\varepsilon}_{p,uni}$ and $\dot{\varepsilon}_{p0}$ are defined based on the quasi-static uniaxial testing rate, as described in Section 2.2. The thermal softening parameters Θ_m, Θ_r and m_x and the specific heat capacity c are found from experiments on similar steels in the literature, as described in Section 2.4.

The damage parameters C_1, C_2, C_3 and D_c (with the linearity assumption of $m = 1$) are found from the fracture behaviour in the tensile (Section 4), Charpy (Section 5) and SENB (Section 6) tests by calibrating them so that the experimental and simulated force–displacement curves agree. This involves simulating the three tests with a given set of damage parameter values, comparing the experimental and simulated force–displacement curves in all three tests, and repeating this while tuning the parameters until the force–displacement curves match for all three tests. Besides matching the overall shape of the force–displacement curves, attention is given to capturing the occurrence of slant fracture and agreement between the simulations and experiments in the fracture elongation A, the Charpy energy C_v and the maximum force of the SENB test to within 5 %. The implication of this calibration approach is that only the 5 damage parameters require calibration using finite-element simulation of only 3 tests' response histories, while the rest are taken directly from either the tensile test mechanical properties (σ_y, σ_u, $\varepsilon_{sh,p}$, ε_u) or from empirical relations (strain rate data).

Additionally, deeper investigation into the relevance of the triaxiality dependence and the nature of the softening parameters, as discussed in Section 7, reveals that this calibration procedure can be further reduced to be based on only 2 key parameters, C_2 and C_3, instead of all 5 damage parameters, for specific groups of steels with weak triaxiality dependence. In terms of the calibration effort required, this is an improvement from the approaches used for other coupled viscoplastic damage models. For example, Novokshanov's [32] drop-weight tear test (DWTT) modelling approach involved 7 damage parameters and calibration to 9 different test specimen geometries. Another point of reference is Simha's [33] DWTT modelling approach, which involved 8 damage parameters and calibration to only 3 tests but which also relied on adopting 6 damage parameter values from previous calibration of a specific steel. The present approach has a smaller number of calibration parameters, requires a smaller number of tests, and does not rely on damage parameter values obtained from calibrations of other materials.

The present model was separately calibrated for an S690QL [38] steel and an AH36 [39] steel to validate its capability to describe the behaviour in the 3 different mechanical tests simultaneously for a given material. The S690QL steel had a nominal thickness of 12 mm and a measured thickness varying between 12.35 and 12.80 mm. The AH36 steel had a nominal thickness of 11 mm and a

Table 1
Material parameter values for the S690QL and AH36 steels assumed in the simulations shown in Sections 4 to 7.

(a) Plasticity and damage.

		AH36	S690QL
σ_y	[MPa]	381	836
$\epsilon_{sh,p}$	[–]	0.0138	0.0438
ϵ_0	[–]	0.0077	0.0413
K	[MPa]	794.0	984.1
n	[–]	0.0141	0.0192
C_1	[–]	0.20	0.47
C_2	[–]	1.90	8.50
C_3	[–]	0.20	0.47
m	[–]	1	1
D_c	[–]	1.3	1.3

(b) Rate dependence, thermal effects and elasticity.

		AH36	S690QL
C	[s^{-1}]	17 070.3	40 524.5
q	[–]	5.2	3.3
$\dot{\epsilon}_{p,uni}$	[s^{-1}]	0.00025	0.00025
$\dot{\epsilon}_{p0}$	[s^{-1}]	0.00025	0.00025
Θ_m	[°C]	1500	1527
Θ_r	[°C]	25	20
m_x	[–]	0.8	1.071
c	[J/kg/°C]	480	452
E	[MPa]	208 767	206 064
ν	[–]	0.3	0.3

measured thickness varying between 10.95 and 11.05 mm. Uniaxial tensile, Charpy and SENB specimens were made using electrical discharge machining and then tested at ambient temperature.

The specimens were modelled using C3D8R elements in Abaqus [77], which are 8-noded hexahedral elements with reduced integration and hourglass control. The density ρ of steel was assumed to be 7850 kg m^{-3}. In the simulations of the quasi-static tests, mass scaling was applied in order to model the tests within a reasonable computation time. The simulations were checked to ensure that no inertial effects large enough to influence the solution significantly were introduced. The kinetic energy was less than 1 % of the total internal energy except for the very brief period at the beginning in which the load application boundary first moves and the deformations are very small in comparison to the movement. No mass scaling was applied in the simulations of the dynamic Charpy tests. A coefficient of friction of 0.15 was assumed for the contact between the specimen and the external contact surfaces in the Charpy and SENB tests, with the exception of the two SENB support rollers, which were considered to be frictionless.

In the calibration process, it was seen that different calibration parameters led to different simulated fracture morphology, including fully flat, fully slanted and in-between situations with different amount of flat and slant fracture. However, the relationship between the calibration parameters and the transition behaviour between flat and slat fractures is outside the scope of the present study, and several other works in the literature have been dedicated to that topic (e.g. [83–85]). All test repetitions experienced some degree of slant fracture, and as will be seen in the following sections, all the calibrated simulations had slant fracture surfaces similar in character to that observed in the experiments, although the slant fracture area in the simulations was not always the same size as that observed in the experiments. In this regard, capturing the occurrence of slant fracture is used as an indicator that the correct mechanism is being modelled and gives confidence to the calibration and the validity of the simulations.

Table 1 shows the parameter values for each steel, including the calibrated C_1, C_2, C_3, m and D_c, which capture the behaviour in the three tests well. The detailed results and discussion for each of the simulations are shown in Sections 4–6, respectively.

4. Uniaxial tensile test

Uniaxial tensile tests were performed according to EN-ISO-6892-1 [46] on 5.5 mm and 6.0 mm thick (approximately half-thickness) specimens machined from the AH36 and the S690QL plates, respectively. The transverse material direction was tested; i.e. the rolling direction was perpendicular to the longitudinal axis of the specimens. Flat proportional dog-bone specimens with a standard width of 25 mm as given in IACS URW [86] were used. Table 2 shows the parallel length L_c, gauge length L_0, width W and thickness B of the specimens.

Only half the width of the specimen was modelled to save computational time, but the full specimen thickness and length up to a third of the grip area was considered in order to capture the asymmetric slant fracture mechanism. A mesh with an element size in the fracture zone of $l_e = 0.1$ mm was chosen as a result of a mesh convergence study, where l_e is the geometric-mean-based characteristic element length, given by the cube root of the undeformed element's volume. Furthermore, a sufficiently low aspect ratio between the longitudinal dimension of the elements and the through-thickness dimension of the elements was required in order to capture slant fracture, as identified by Li and Wierzbicki [28]. In the AH36 tensile test, the ratio was 1/3, while in the S690QL tensile test which experienced greater straining, this ratio was as low as 1/5.

Table 2
Uniaxial tensile test specimen properties.

	Test prefix	L_c [mm]	L_0 [mm]	W [mm]	B [mm]
S690QL	STT	93.7	69.2	25.0	6.0
AH36	ATT	89.7	66.3	25.0	5.5

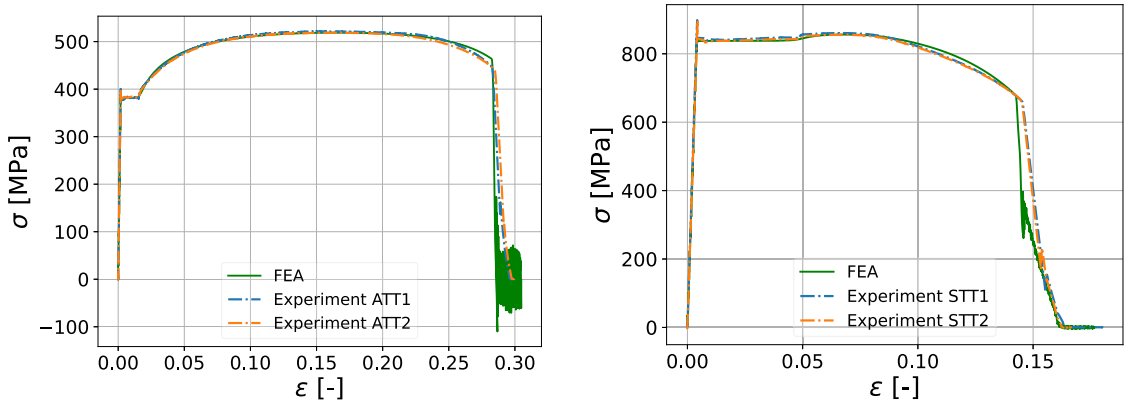

(a) AH36. (b) S690QL.

Fig. 4. Experimental and simulated engineering stress–strain curves.

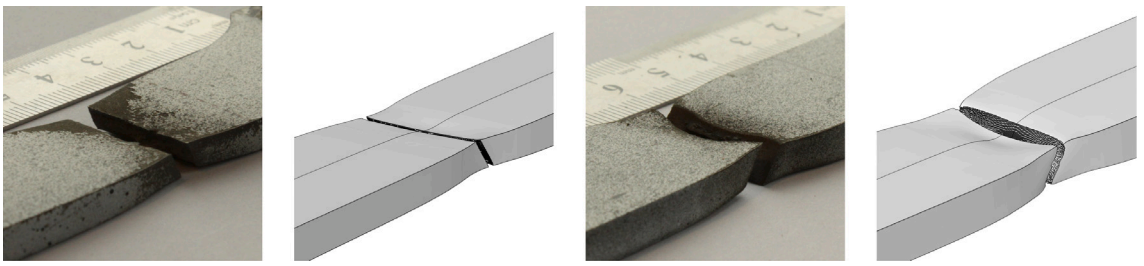

(a) AH36 test ATT1 (b) AH36 simulation. (c) S690QL test STT1. (d) S690QL simulation.

Fig. 5. Fracture morphology in the tensile test.

The use of the hardening parameters n, K and ε_0, calculated from σ_y, σ_u, $\varepsilon_{sh,p}$ and ε_u as outlined in Section 2.1, combined with the empirical rate-dependence behaviour assumed in Section 2.2, which take into account the changing strain rates due to necking [59,87], leads to a good estimation of both the pre-necking behaviour and the post-necking behaviour before the onset of fracture (Fig. 4). The onset of fracture corresponds to the start of the steep drop in the stress, which occurs when the most highly strained elements at the centre of the specimen attain $D = D_c$. However, the damage initiation strains and the attainment of $D = 1$ are seen to play the largest role in determining when this drop occurs, because the material accelerates towards failure once $D = 1$ occurs. The onset of softening and the onset of fracture happens almost simultaneously in these tensile simulations, such that material softening has a small effect in the post-necking, pre-fracture regime. So, the damage parameters are calibrated by choosing parameters for which the onset of fracture and the associated slope of the degradation in the simulation plot close to those of the experiments. The A, defined as the fracture elongation over the proportional gauge length from pieced-together tensile test fragments [46], was calibrated to within ±5 % of the average of the experimental values (Table 3). The minor discrepancy seen in the pre-damage-softening diffuse necking portion of the stress–strain curve could be attributed to the sensitivity of the localisation behaviour to the strain-rate dependence [59,87], and the response in this region could hence be improved by more accurate strain-rate dependence modelling for the individual materials. However, since the focus of the study is on the ductile fracture behaviour, the present empirically derived curve-fitting parameters are assumed for the purpose of capturing the general trend and averaged rate-dependence behaviour for the given steels, and the calibration is performed on the damage parameters.

Fig. 5 shows that the simulation captures key ductile fracture features observed in both the AH36 and S690QL tensile tests, such as a necking zone, through-thickness slant fracture and through-width tapering of the fracture surface. The more pronounced thickness reduction at the centre of the neck observed in the S690QL tensile test than in the AH36 tensile test was also represented in the simulation.

Table 3
Experimental and finite-element comparisons for the tensile test properties.

		AH36			S690QL		
		ATT1	ATT2	FEA[a]	STT1	STT2	FEA[a]
E	[MPa]	204 865	208 767	205 142	214 013	206 064	204 682
σ_y	[MPa]	379	381	381	840	836	837
σ_u	[MPa]	521	518	519	860	855	856
σ_y/σ_u	[–]	0.73	0.74	0.73	0.98	0.98	0.98
ϵ_{sh}	[–]	0.0155	0.0157	0.0147	0.0480	0.0490	0.0389
ϵ_u	[–]	0.1566	0.1630	0.1650	0.0671	0.0668	0.0675
A_e	[–]	0.2967	0.2986	0.2859	0.1635	0.1624	0.1621
A	[–]	0.28	0.29	0.29	0.15	0.16	0.16

[a] Note these are output values from the FEA results and not the input values to the FEA. The input E, σ_y, σ_u, ϵ_{sh} and ϵ_u for AH36 and S690QL simulations are taken from the experiments ATT2 and STT2, respectively, which result in the hardening parameters shown in Table 1.

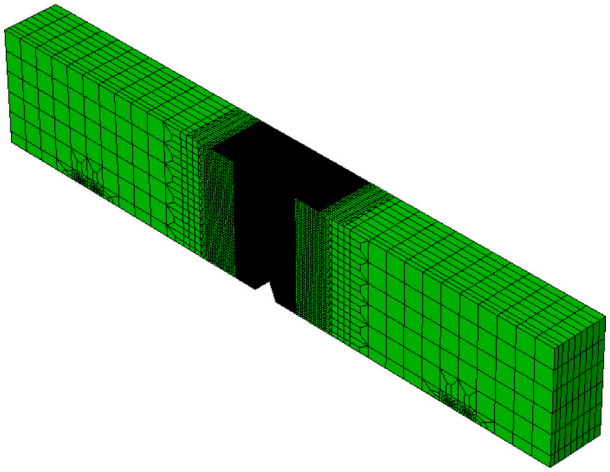

Fig. 6. Half model of Charpy specimen with mesh refinement.

5. Charpy impact tests

Three instrumented Charpy impact tests [35,88] were performed on each steel grade for the transverse direction of the material, resulting in Charpy impact energies as given in Table 4. An MTS-E22 instrumented Charpy testing machine set up with a pendulum mass of 32.85 kg, a pendulum energy of 450 J and a striking speed of 5234 mm s^{-1} was used. Half of the Charpy specimen was simulated (Fig. 6), with a plane of symmetry at half thickness, so that slant fracture could be captured. The mesh was refined in a mesh convergence study resulting in a chosen characteristic length l_c of ~0.06 mm for the elements directly above the notch.

For each steel grade, the force–displacement plot (Fig. 7) of the test giving the median impact energy of the three is used for calibration of the material parameters. The energies calculated from the force–displacement extracted from the finite-element simulations were within 5 % of the corresponding experimental Charpy impact energies (Table 4). Fig. 7 shows both the simulations with and without thermal softening due to adiabatic heating. It is seen that adiabatic heating has a negligible effect on the force–displacement curve for the AH36 simulation, while in the S690QL simulation, the effect is significant and serves to greatly improve the quality of the material model calibration, considering that a good calibration necessitates capturing the behaviour in the Charpy, SENB and tensile test simultaneously, and the SENB and tensile tests are assumed to be isothermal. The effect being greater in the S690QL steel correlates with the significantly higher notch toughness and Charpy impact energy of the S690QL steel in comparison with the AH36 steel (Table 4), since the adiabatic heating is caused by the dissipated energy. This also corroborates the findings in studies by Tanguy et al. [68] and Seo et al. [69] that the adiabatic heating effect should not be neglected in simulations of ductile Charpy tests, despite the widely adopted practice in existing work on ductile Charpy modelling, e.g. [18,89–92], to neglect it. Hence, the adiabatic heating should be considered at least for ductile Charpy tests with high C_v.

Fig. 7 shows that the general shape of the force–displacement response was captured, although the post-peak drop in the force for the S690QL simulation occurred earlier than in the experiment. Figs. 8 and 9 show that the simulation captures the characteristic shear lips observed in both the AH36 and S690QL Charpy tests, although the amount of slant fracture was not accurately represented. The simulations predict larger shear lips in the AH36 than in the S690QL Charpy tests, while the reverse is seen in the experiments. The FEA correctly predicted a full separation of the specimen for the AH36. However, it underpredicted the amount of remaining ligament in the S690QL Charpy test, giving a response in which the specimen is just on the verge of full separation by the end of the test, while the specimen remains in one piece in the experiment. The calibration process focused on capturing the C_v and

Table 4
Experimental and simulated Charpy impact energies from the instrumented Charpy tests.

	Experimental C_v [J]				FEA C_v [J]	
	1	2	3	mean	adiabatic	isothermal
AH36	51.1	49.7	38.8	46.5	47.2	48.4
S690QL	197.2	217.7	204.2	206.4	209.4	223.2

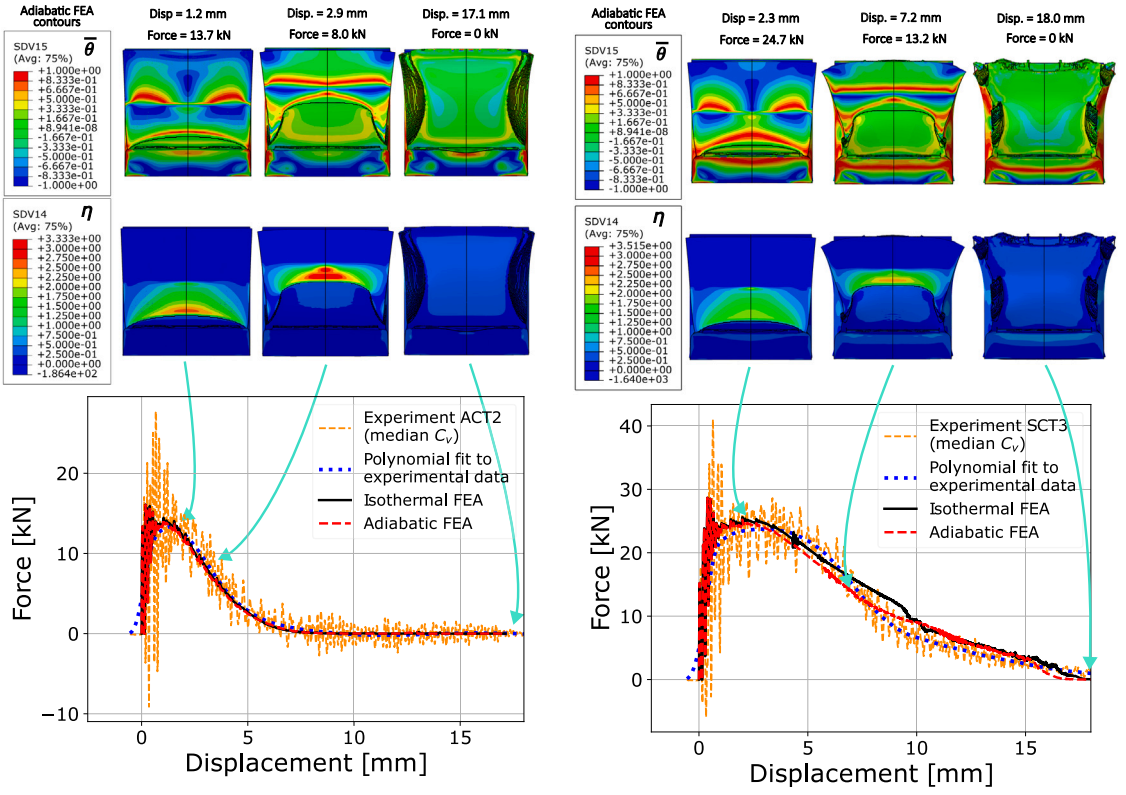

(a) AH36. (b) S690QL.

Fig. 7. Experimental and simulated Charpy impact force–displacement curves.

general shape of the force–displacement curve, since these are the more readily information available from Charpy tests in practice, particularly the C_v, such as is found in mill test certificates. The ability of the model to produce the approximate form of the shear lips gives confidence that the appropriate mechanism and stress state distribution shape are being accounted for. The contour plots of the stress state distributions will be discussed in more detail in comparison with the SENB fracture behaviour in Section 7.3.

While the fracture surface of AH36 shown in Fig. 8(c) is shiny and mostly flat, fractography with a scanning electron microscope has confirmed that it failed in a ductile, void-dominated failure mode.

6. Single-edge notched bending test

Full-thickness SENB tests were performed on the AH36 and S690QL steels according to ASTM E1820-23b [93]. The materials were tested in the direction transverse to the rolling direction; i.e. the material's transverse direction was aligned with the longitudinal axis of the specimen. Table 5 shows the thickness B, width W, length L, notch-mouth opening N, notch width w, notch length a_n, measured initial cracked length a_0, compliance-estimated initial crack length a_{0q}, measured physical crack extension Δa_p and the compliance-estimated crack extension Δa_{pq} from the SENB tests. The fracture surface and the crack extension measurements are shown in Fig. 10.

For simplicity, the initial fatigue crack in the simulations was modelled as a flat straight-through crack with a constant through-thickness length equal to the measured a_0. The sharp crack tip ended in a node, as shown in Fig. 11. The mesh was refined in a

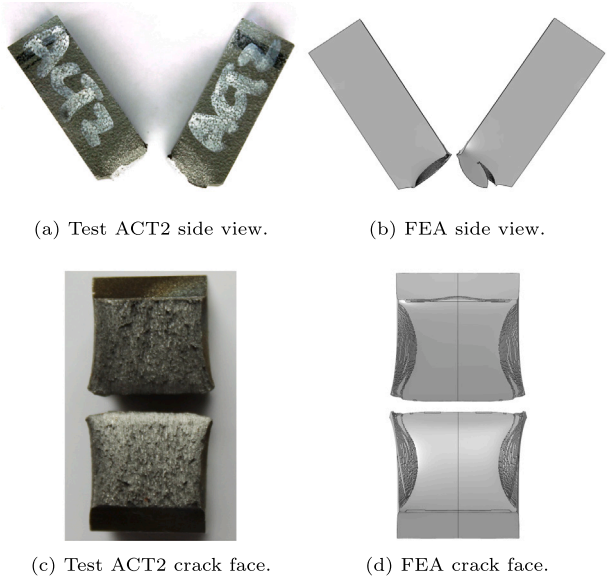

(a) Test ACT2 side view. (b) FEA side view.

(c) Test ACT2 crack face. (d) FEA crack face.

Fig. 8. Fracture morphology in the AH36 Charpy test.

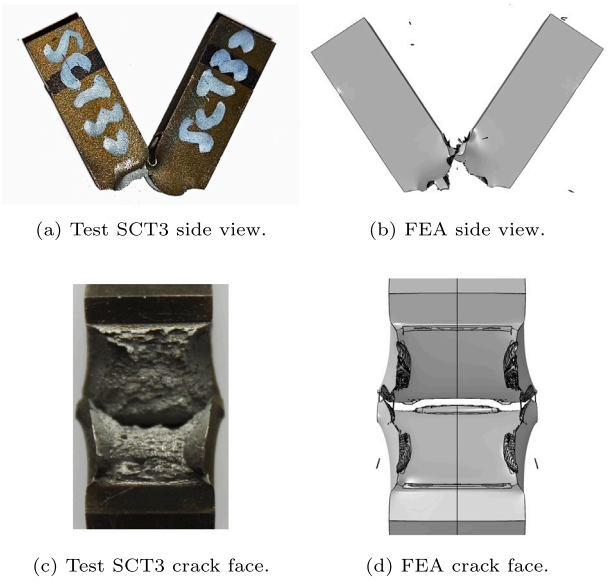

(a) Test SCT3 side view. (b) FEA side view.

(c) Test SCT3 crack face. (d) FEA crack face.

Fig. 9. Fracture morphology in the S690QL Charpy test.

Table 5
Single-edge notched bending specimen properties.

Grade	Test name	B	W	L	S	N	w	a_n	a_0	a_{0q}	Δa_p	Δa_{pq}
		All in [mm]										
AH36	AST3	10.9	21.9	101.1	88.0	3.0	0.32	9.7	12.47	12.57	2.57	1.42
S690QL	SST3	12.3	24.0	110.3	96.0	3.0	0.32	10.7	14.93	15.17	0.70	0.85

mesh convergence study resulting in a chosen characteristic length l_c of ~0.08 mm for the elements in the crack area. Like the Charpy simulation, a half model with a plane of symmetry at half thickness was used so that slant fracture could be captured (Fig. 12).

The unloading compliance method based on the crack-mouth opening displacement (CMOD) was applied to both the experiments and the simulations in order to obtain force-CMOD (Fig. 13) and $J - \Delta a$ curves (Fig. 14). Bending and rotation corrections for the SENB calculations paired with Bakker's [94] compliance equations as suggested by Wallin [95] were used.

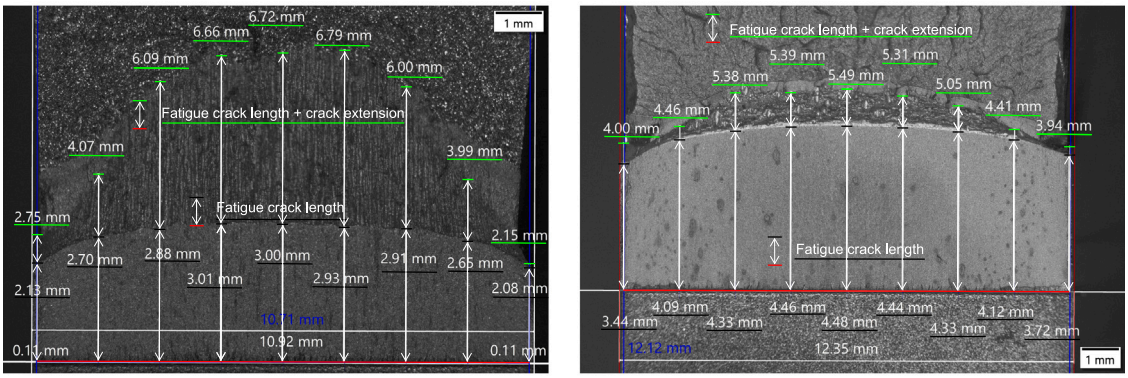

(a) AH36. (b) S690QL.

Fig. 10. Crack length measurements.

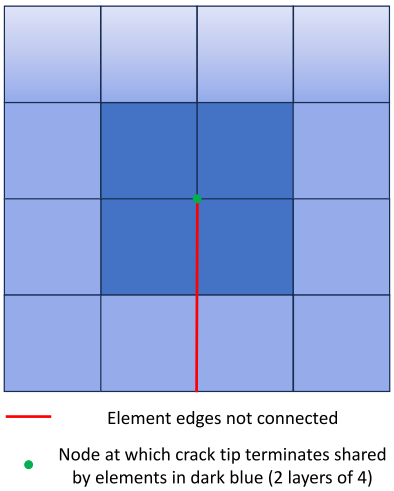

Fig. 11. Schematic cross-section showing the meshing around the crack tip.

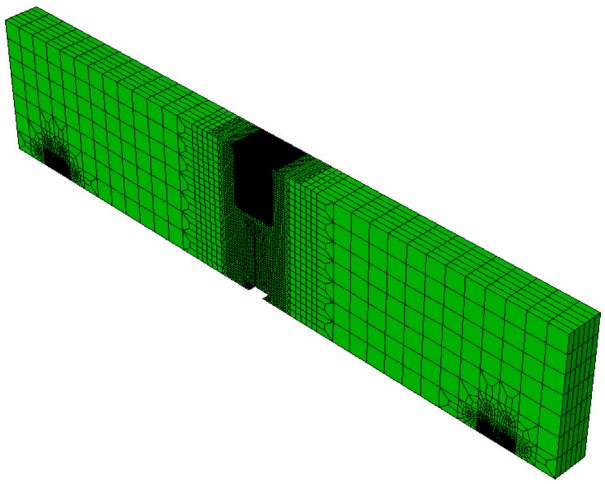

Fig. 12. Half model of SENB specimen with mesh refinement.

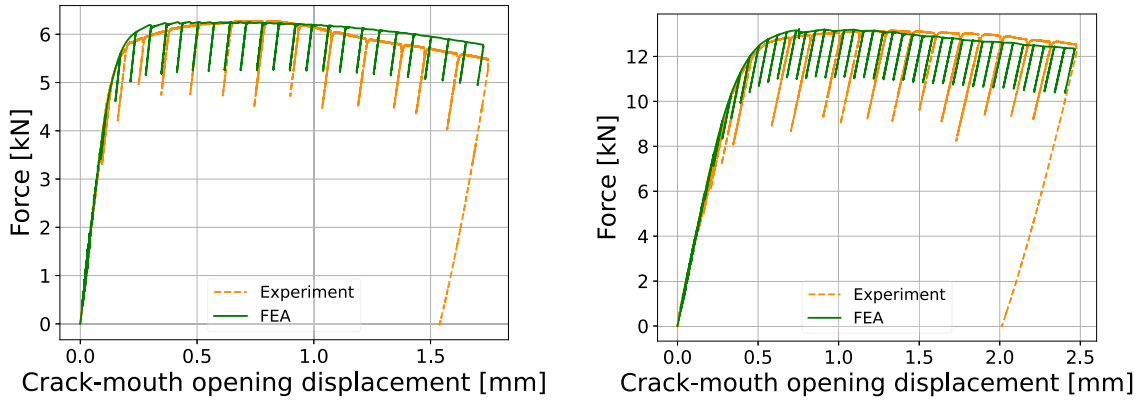

(a) AH36. (b) S690QL.

Fig. 13. Experimental and simulated F-CMOD curves.

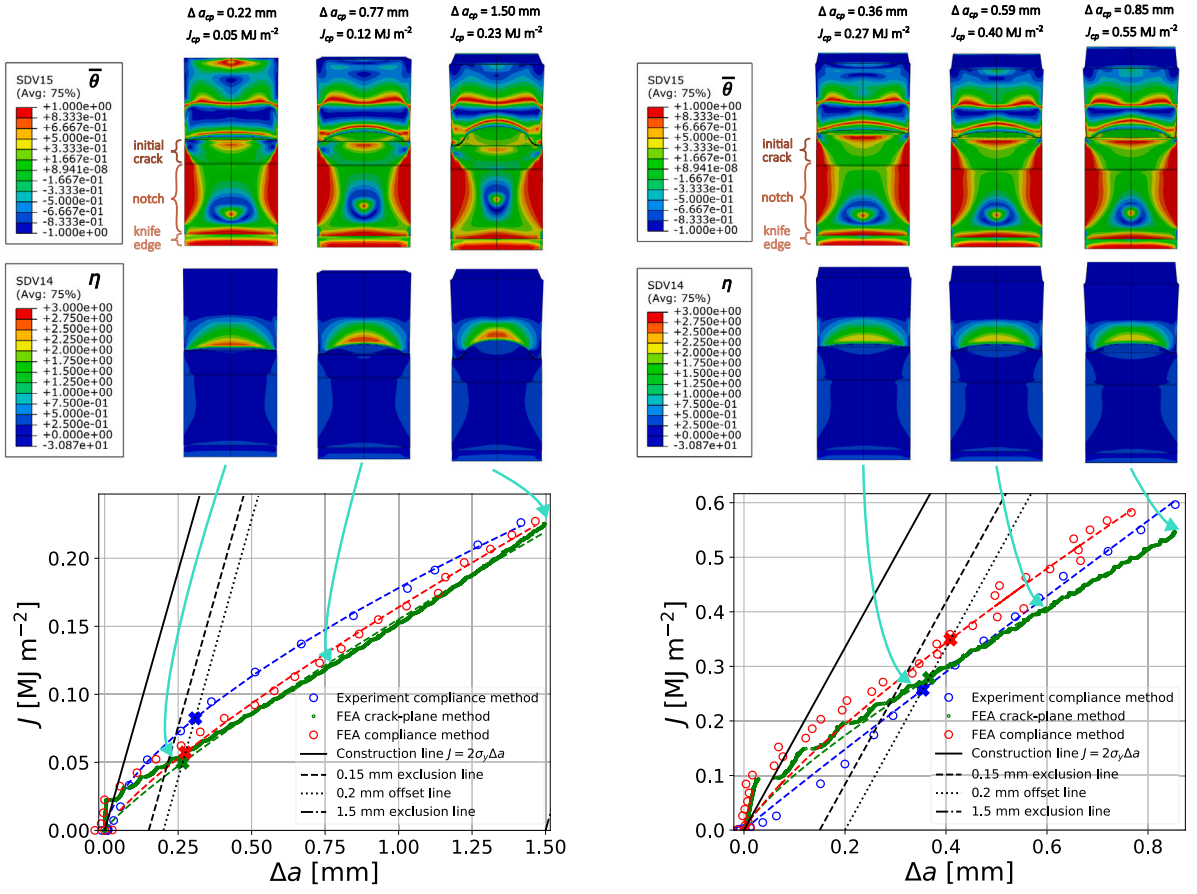

(a) AH36. (b) S690QL.

Fig. 14. Experimental and simulated $J - \Delta a$ curves.

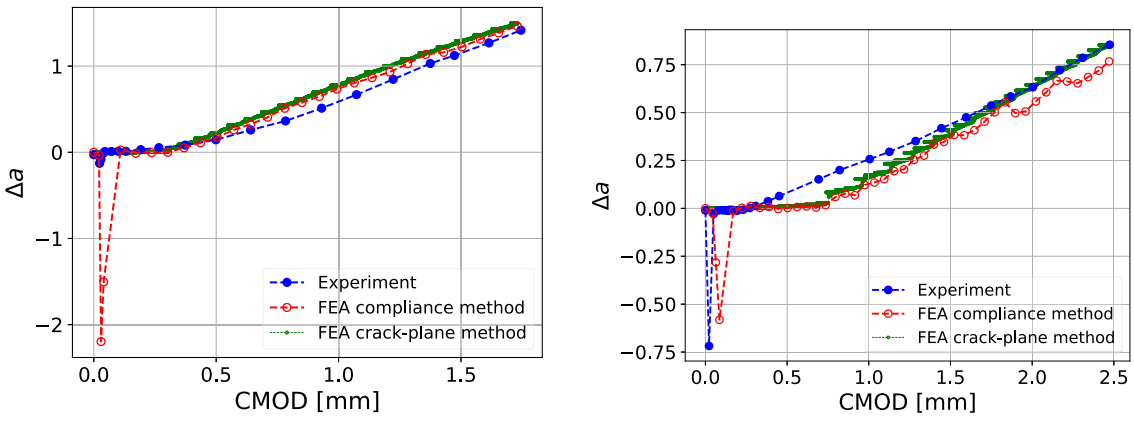

(a) AH36. (b) S690QL.

Fig. 15. Experimental and simulated Δa - CMOD curves.

The early-stage crack length estimates obtained from the compliance method applied to the finite-element simulation resulted in an underestimation of a of up to ~2 mm at low CMOD (Figs. 15(a) and 15(b)) in comparison to the physically measured a_0 which was also assumed in the simulation. This could be attributed to the inadequacy of the applied compliance methodology for capturing initial crack-tip blunting [96] as well as the discrepancy between the actual curved initial crack front (Fig. 10) and the assumed flat initial crack front in the simulation. Therefore, the ASTM E1820-prescribed [93] adjustment for a_{0q} was applied using the (a, J) data points excluding those determined at forces below the maximum precracking force, instead of using all the (a, J) data points below the maximum achieved force. The crack growth values (Fig. 15) were calculated with respect to the corrected a_{0q}, and a power curve was then fitted to the data points excluding Δa values outside of the 0.15 mm exclusion line in order to determine the critical J_Q from the intersection with the 0.2 mm offset line, according to standard procedure [93]. This excludes the early nonlinearities and crack-tip blunting effects, which make early compliance-based a values non-realistic, from the determination of the J_Q. This procedure likewise reduces the effects of the discrepancy in the simulated early-stage crack front geometry on the construction of the $J - \Delta a$ curves.

The loss of stiffness in the SENB simulations is brought about by the material softening and element deletion that lead to a weakened and reduced cross-section in the simulated SENB specimen. Degradation in the elastic behaviour has not been accounted for, but the level of agreement between the experiments and the simulations in the compliance-based calculations [93] of the crack lengths (Fig. 15) suggests that the degradation in the flow stress accounts for the greater part of the stiffness degradation, such that degradation in the elastic behaviour may be neglected for the present purposes. If damage softening represents the void nucleation, growth, and coalescence mechanism, then it is reasonable to expect that damage softening could also be applied to the elastic parameters, but this was not evaluated in this study.

Crack lengths were also extracted from the finite-element model based on the crack plane formed by the deleted elements. The crack extension Δa was calculated by dividing the area formed by the deleted elements by the minimum width at the crack plane, which was found to give similar Δa values (within 0.05 mm) as the nine-point method. The force-CMOD compliance needed in the procedure for calculating J values were estimated from the FEA area-based Δa using the conversions given by ASTM E1820 [93]. The results are shown in Figs. 14 and 15 under the label 'FEA crack-plane method'.

Figs. 13 and 14 and Table 6 show relatively good overall agreement between the finite-element and experimental results. The calibration was performed based on the force–displacement curve (Fig. 13), hence the greater variance between the experimental and simulated J-Δa (Fig. 14) than between the experimental and simulated force–displacement curves. Nonetheless, the simulated J-Δa curves perform surprisingly well considering the low number of unique testing conditions (3) used for calibration of the damage parameters in comparison to that seen in the modelling of similar tests in other works (6 in [96] and 4 in [97]). Other than the purposeful simplification of the material model and calibration procedure, the difference in the experiments and simulations could also be attributed to geometrical simplifications, such as the flat instead of curved shape of the assumed initial crack front and the subsequent difference in crack front shapes between the experiments (Fig. 10) and simulations (Fig. 14). The rollers in experiment rolling away from each other also slightly changes the span between the rollers, while the inter-roller distance is fixed in the simulation.

Fig. 16 shows that the FEA captures slant fracture behaviour seen at the free surface of the tests. However, the slant fracture occurs relatively late in the test, such that it does not have much effect on greater part of the J-Δa curve. This and the tunnelling behaviour as shown in Figs. 10 and 14 will be discussed in more detail in Section 7.3 in relation to the Charpy tests.

7. Discussion

This section discusses key insights found from the modelling and calibration process which could help reduce the calibration effort in certain useful future situations concerning Charpy and fracture toughness correlations. First, the suitability and effectiveness of

Table 6
Experimental and finite-element comparisons for the SENB test.

		AH36		S690QL	
		AST3	FEA	SST3	FEA
F_{max}	[kN]	6.27	6.26	13.15	13.41
J_Q compliance	[MJ m^{-2}]	0.082	0.057	0.257	0.349
J_Q crack plane	[MJ m^{-2}]	–	0.050	–	0.279

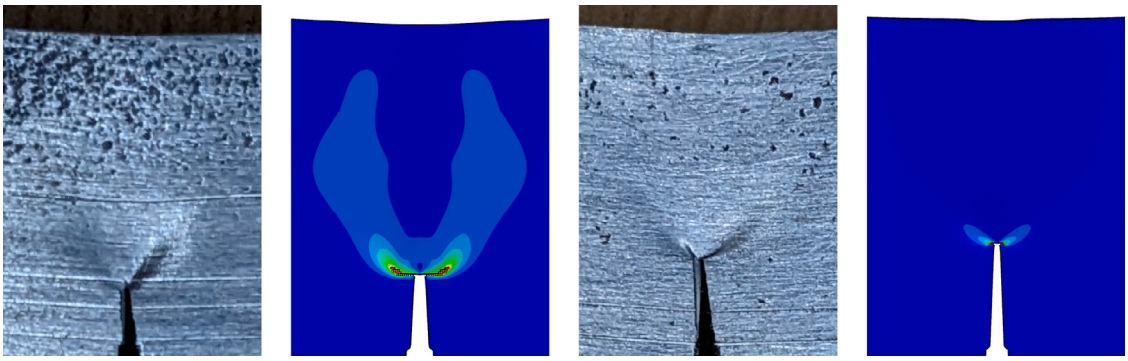

(a) AH36 test AST3. (b) AH36 simulation. (c) S690QL test SST3. (d) S690QL simulation.

Fig. 16. Slant fracture in the SENB test.

the triaxiality independent assumption for the range of stress states involved in these simulations is exemplified for the present steels with weak triaxiality dependence (Section 7.1). The useful similarity in the softening parameters between similar steels observed in the present work and in the literature is noted (Section 7.2). Consequently, it is shown how the calibration procedure could be reduced to be based on only 2 key parameters, C_2 and C_3, instead of all 5 damage parameters. Finally, the similarities and differences in the crack propagation behaviour in the Charpy and SENB fracture toughness tests are discussed, highlighting in particular how both display a similar tunnelling behaviour and a similar stress state evolution at key locations (Section 7.3).

7.1. Triaxiality and lode angle dependence (C_1, C_2 and C_3)

Sections 4 to 6 show that the present model is capable of capturing the behaviour in the different mechanical tests of the AH36 and S690QL steels accurately using a fracture strain locus which is triaxiality-independent ($C_1 = C_3$), although metals are frequently found to fracture at smaller strains when subject to higher stress triaxiality [25,98]. According to Xue's [99] investigation of Bridgman's experiments [98] on high-strength steels using a stress-based pressure- and Lode angle-dependent fracture criterion, the pressure sensitivity of steels decreases with decreasing hardenability, increasing yield stress and increasing reference fracture strain (defined at $(\eta, \bar{\theta}) = (0, 1)$). Hence, the present steels under investigation can be expected to have low pressure dependence due to the high fracture strains of both the AH36 and S690QL and the low hardenability of the S690QL, and this is corroborated by the efficacy of the present stress-independent calibration of the fracture strain locus.

It is also worth noting that although the maximum triaxiality near a sharp crack tip is high ($\eta = 2.5$ [66] in the perfectly plastic, plane-strain case), much of the damaging behaviour throughout the straining history of a typical element in the crack path of the SENB and Charpy specimens is associated with lower triaxialities due to blunting effects [100]. Fig. 17 shows that for elements with initially high triaxialities in the mid-thickness crack propagation path of the SENB and Charpy tests, the triaxialities drop off after the peak at a low D and has an average[3] η between around 1.1 and 1.3 (Table 7; 0.8 mm above tip). The stress evolution for an element at the initial crack tip as well as an element at an arbitrary distance of 0.8 mm above the initial crack tip is observed, because material at different distances from a crack or notch tip experience different regimes of behaviour in terms of stress states [100–102]. (0.8 mm corresponds to roughly 5 times the experimentally determined 0.2 mm offset critical CTOD of the AH36 and 8 times that of the S690QL). For the tensile test, the average triaxiality of the centroidal element is around 0.5 in the AH36 and 0.7 in the S690QL due to different extents of necking which cause the triaxialities to increase from their initial value of 0.33. The average triaxialities of the key elements in the different tests varying between this smaller-than-expected range of 0.5 and 1.3, combined with the trend of the pressure dependence to be weaker in higher triaxiality ranges than in the lower triaxiality ranges as shown by Xue [99], limits the effect of the material's pressure dependence on the behaviour in these tests.

[3] The averages are calculated only over the range of $0 \leq D \leq 1$, because once D reaches 1, deletion is imminent, with softening causing the plastic straining to accelerate and the von Mises stress to approach zero, which in turn causes the η to approach infinity.

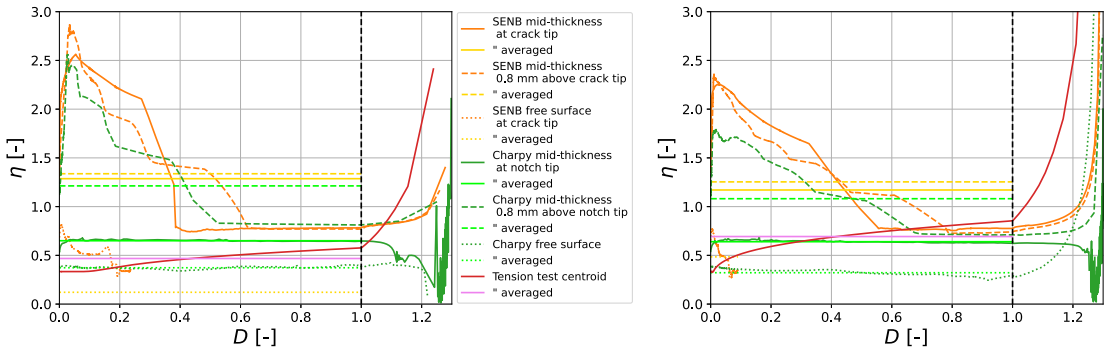

(a) AH36. (b) S690QL.

Fig. 17. Evolution of the triaxiality in key elements in the simulations. Unloading periods in the SENB simulations are omitted.

Table 7
Average triaxialities and Lode angles calculated over $0 \leq D \leq 1$ in key elements in the AH36 simulations.

	Plane	Element	AH36		S690QL	
			η	$\bar{\theta}$	η	$\bar{\theta}$
Tensile test	Half-thickness	Centroid	0.47	0.67	0.69	0.34
Charpy test	Half-thickness	Notch tip	0.65	0.04	0.64	0.02
	Half-thickness	0.8 mm above notch tip	1.21	0.03	1.08	0.04
	Free surface	Notch tip	0.37	0.92	0.32	0.74
SENB test	Half-thickness	Crack tip	1.29	0.02	1.25	0.00
	Half-thickness	0.8 mm above crack tip	1.34	0.01	1.25	0.00
	Free surface	Crack tip	0.51	0.65	0.48	0.67

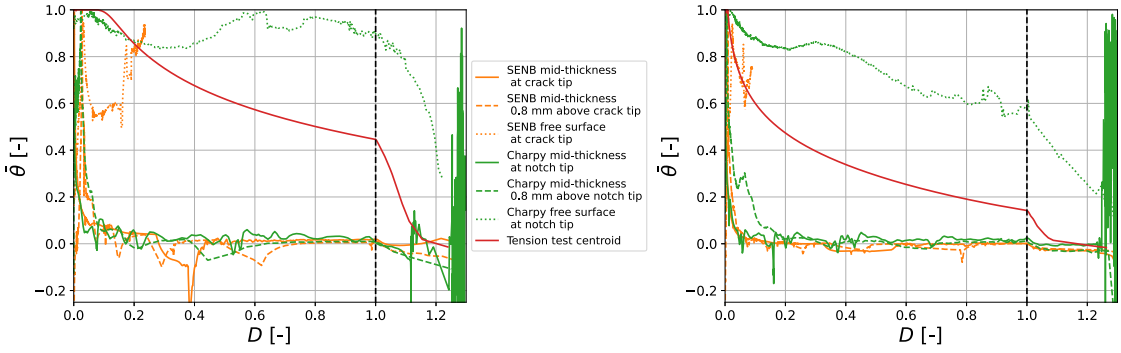

(a) AH36. (b) S690QL.

Fig. 18. Evolution of the Lode angle in key elements in the simulations. Unloading periods in the SENB simulations are omitted.

At the same time, observations have been made by Xue [99] using his stress-based model as well as existing experiments [103, 104] that a lower strain hardening capacity is accompanied by an increase in Lode-dependence in the fracture strains. From Fig. 18, it is clear that there are regions that are dominated by significantly different deviatoric stress states in the test, such as $\bar{\theta}$ close to 0 at the half-thickness symmetry and $\bar{\theta}$ close to 1 at the free surface in the SENB and Charpy specimens, such that this Lode-dependence in the fracture strain will have a significant effect of the fracture behaviour.

It is seen that for the present steels, pressure sensitivity is low and Lode-dependence plays the key role of distinguishing the fracture behaviour observed in different geometries, such that the assumption of a Lode-dependent only fracture strain surface is sufficient for describing the behaviour in different mechanical tests to within reasonable accuracy. This quality has also been observed in Clausing's experiments on several structural steels [99,103] and Banabic's experiments [105,106] on aluminium alloy. Other examples of the successful use of Lode-dependent, triaxiality-independent ductile fracture models (primarily the maximum shear stress (Tresca) model) include applications to tests involving moderate triaxialities between 0.3 and 1 [80,99,107–111] and even higher triaxialities such as in the compact tension test [112] and the Charpy impact test [36]. However, these (except for [36])

primarily involved the simulation of sheet metals subject to plane stress, in which the triaxiality dependence is implicitly accounted for through the one-to-one relationship between the Lode angle and triaxiality [80,112], regardless of the pressure sensitivity of the metal's fracture behaviour.

The major advantage of assuming triaxiality independence is the reduction of the number of calibration parameters and the model calibration effort while still capturing the slant fracture mechanism and the force–displacement response in key tests for low-pressure-sensitivity steels, at the cost of a slightly reduced model accuracy. Nevertheless, it should be noted that such models cannot capture the behaviour in axisymmetric [80,107] tests and should only be used for steels with low triaxiality dependence in the range of the triaxialities of interest. For example, it would not work for very-low-triaxiality-dominated, pressurised situations [98] (before the cut-off value [67]), because even metals with low pressure sensitivity in the medium to high triaxiality ranges are generally pressure-sensitive in the very-low-triaxiality range [99].

7.2. Softening parameters (m and D_c)

For simplicity, a linear relationship is assumed for the decay of β with respect to D, such that $m = 1$. The present value of $D_c = 1.3$ for both AH36 and S690QL (both hot-rolled low-carbon structural steel plates) is close to the only other application of this version of the softening model to a hot-rolled low-carbon structural steel plate found in the literature [113], which was $D_c = 1.2$ for Q460C steel. This is significant because a trend has been identified [63] where calibrations of the softening model to different low-alloy steel pipes (X65, X70 and X100) repeatedly resulted in similar values of D_c, ranging from 2.1 to 2.3 [62,96,114]. Similarly, the two existing calibrations to the nickel–chromium Inconel alloy have resulted in D_c values close to each other, i.e. 1.2 [115] and 1.4 [97].

7.3. Similarities and differences between the charpy and SENB fracture behaviour

The evolution of the triaxiality in a typical element in the crack path above the notch tip of the Charpy and the crack tip of the SENB specimen (Fig. 17) reveals that when tunnelling starts, the triaxialities experienced in the Charpy test and the SENB are closer than would be expected based on the different sharpness of the initial crack and initial notch. Only the triaxialities of the elements at the Charpy notch tip and SENB crack tip are significantly different, where the average triaxialities in the AH36 simulations are 0.65 and 1.29, respectively, due to the difference of the notch versus crack geometry, with similar values seen in the S690QL simulations (Table 7). However, the other elements above the Charpy notch tip experience a very similar triaxiality evolution and tunnelling process to that occurring in the SENB test. This is also seen in the η distribution shown in the second row of contour plots in Figs. 7 and 14.

In Figs. 7(a) and 7(b), the first column of contour plots corresponds to a frame close to the occurrence of the maximum force, the second column corresponds to a frame where around 70 % of the Charpy impact energy has been dissipated, and the third column corresponds to the end of the simulation. In Figs. 14(a) and 14(b), the first column of contour plots corresponds to a frame close to the occurrence of the 0.2 mm offset J_Q; the third column corresponds to the end of the simulation, which is at the end of an unloading period after the simulated CMOD reaches a value close to them maximum CMOD achieved in the experiment; and the second column corresponds to a crack extension roughly halfway in between those of the two other columns. These figures show that the slant fracture in the SENB test only occurs to a small extent towards the end of the simulation, such that the J_Q and the majority of the greater part of the J-Δa curve is not affected by slant fracture, while more extensive slant fracture is seen to occur in the Charpy test. Despite this, the stress states caused by the tunnelling geometry dominates the behaviour of most of the duration of the Charpy test. Even when 70 % of the C_v has been dissipated, the amount of slant fracture in the Charpy simulations is still relatively small, such that the stress state distributions in the both Charpy and the SENB simulations are still mainly determined by the tunnelling that occurs in both simulations. This can be seen by comparing the first and second columns of the contour plots in Figs. 7(a) and 7(b) with the contour plots in Fig. 13.

These plots also reveal that the Charpy simulation experiences purely tunnelling behaviour with no slant fracture until after the attainment of the maximum force, with the crack first propagating parallel to the initial crack through the whole width including the free surface. In the SENB simulation, the crack at the free surface propagates in a slant direction without first extending parallel to the initial crack. This is why the free surface crack-tip element in the SENB simulation is seen in Figs. 17 and 18 to accumulate only a small amount of damage D before it stopped straining altogether: slant fracture starts in the element right below that, causing the crack not to progress parallel to the original crack (Fig. 16).

Therefore, the correlations between ductile C_v and J values are strongly related to the similar extensive tunnelling behaviour that occurs in the two tests, and the key difference that has to be accounted for in modelling the two correctly is capturing the rate dependence, thermal softening and dynamic effects in the Charpy test.

8. Conclusions and recommendations

A coupled rate-dependent plasticity model with damage softening and thermal softening has been presented and validated for the purpose of correlating Charpy V-notch toughness and SENB fracture toughness. Its ability to be calibrated using only the tensile, Charpy notch impact and SENB fracture mechanic tests and to simulate the force–displacement behaviour and ductile fracture characteristics in all these three tests simultaneously has been demonstrated for AH36 and S690QL steel.

The suitability and effectiveness of various simplifications to the model for the purpose of practical engineering application have been substantiated. Sections 7.1 and 7.2 have outlined how triaxiality independence and empirical softening parameters can be assumed for certain steels to reduce the number of damage initiation parameters to two. Section 7.3 has demonstrated the strong similarities in the tunnelling behaviour and stress-state distributions in the Charpy and SENB tests at key locations and at key extents of progression of the tests, giving insight into the mechanical basis for the correlations between the two tests. These insights could also be used to reduce the calibration effort of damage mechanics models for these tests, given that the key differentiating factors of rate-dependence and adiabatic heating are correctly accounted for, since a calibration to the Charpy test effectively involves calibrating to a stress-state distribution and evolution range that is almost the same as that of the SENB test.

With this, a material modelling and calibration approach for the mechanics-based correlation between notch toughness in Charpy impact tests and fracture toughness in SENB tests has been established. Finally, it is worth noting that given its purpose, the approach has not been validated for the application to other mechanical tests and other stress state ranges: the calibration involves simplifications specifically effective for reducing calibration effort without sacrificing the ability to capture the behaviour in specifically these three tests. The future research outlook provided by the current work is to calibrate the model for various weakly triaxiality-dependent steels using widely available Charpy and tensile test properties, in order to predict how the fracture toughness from the SENB varies with these properties, providing numerically derived mechanics-based correlations between C_v and J.

Two other notable findings peripheral to the central argument have been observed in the course of this work. First, the importance of the adiabatic heating effect for Charpy tests with high impact toughness and hence high C_v has been shown, while this effect has been observed to be negligible in the ductile Charpy tests with low C_v. This provides nuance to the existing discussion in the literature, in which a few have recently pointed out the importance of accounting for this effect, while many more have shown good results even while ignoring it (Section 5). Second, the analytical approach of finding the plastic hardening curve parameters using the Considère criterion and only key points from the engineering stress–strain curve, being the yield stress, the length of the yield plateau, the ultimate stress and the uniform elongation, instead of the full engineering stress–strain curve, has proven to be effective for modelling the behaviour up to the necking point. This leads to the recommendation to include the reporting of yield plateau length and uniform elongation in the mill test certificates, enabling the modelling of pre-necking behaviour using only point data from the mill test certificate.

CRediT authorship contribution statement

Wei Jun Wong: Writing – original draft, Visualization, Validation, Software, Methodology, Investigation, Formal analysis, Data curation, Conceptualization. **Carey L. Walters:** Writing – review & editing, Supervision, Resources, Project administration, Methodology, Funding acquisition, Conceptualization.

Declaration of competing interest

The authors declare that they have no known competing financial interests or personal relationships that could have appeared to influence the work reported in this paper.

Acknowledgements

The authors gratefully acknowledge the funding provided by the consortium of companies consisting of Bureau Veritas Marine & Offshore SAS, Damen Schelde Naval Shipbuilding BV, Huisman Equipment BV, Lloyd's Register EMEA, POSCO, as well as the Topconsortia voor Kennis en Innovatie (TKI). The authors thank Virginia Bertolo, Elise Reinton and Ton Riemslag of the Mechanical Behaviour Lab at TU Delft for lending and assisting with the use of their experimental equipment, and Marcelo Paredes from Texas A&M University for the helpful discussions about damage softening.

Appendix. Stress-update algorithm for viscoplastic consistency model with damage softening and thermal softening

This is an implementation of the viscoplastic consistency model given by Wang et al. [40] coupled with the damage-softening model of Li and Wierzbicki [28], the Cowper–Symonds rate-dependent flow stress model [22], and the Johnson–Cook [41] thermal softening model.

Subscript $j-1$ refers to quantities from the previous (converged) finite-element analysis increment, and subscript $i-1$ refers to the quantities of the previous return mapping iteration of the current increment. Symbols with neither subscript refer to the values from the most recent iteration in the current increment.

To find stress increment for current increment j:

1. Compute trial stress state: $\boldsymbol{\sigma_{trial}} = \boldsymbol{\sigma}_{j-1} + \mathbb{C}\Delta\boldsymbol{\varepsilon}_t$
2. Evaluate yield function $f(\boldsymbol{\sigma_{trial}}, \sigma_{j-1})$

   - If $f \geq 0$: continue to plastic calculations in step 3.
   - Else, check whether this is unloading:

     i. If $\dot{\varepsilon}_{vp,j-1} > 0$: previous increment was plastic; so calculate σ_t using $\dot{\varepsilon}_{vp} = 0$ and re-evaluate $f(\boldsymbol{\sigma_{trial}}, \sigma_t)$. If $f \geq 0$: continue to plastic calculations in 3.

     ii. Else, $\boldsymbol{\sigma} = \boldsymbol{\sigma_{trial}}$ and go to step 6.

3. Initialise zeroth iteration $i = 0$

$$\Delta\lambda_0 = 0$$
$$\dot{\lambda}_0 = 0$$
$$\boldsymbol{n}_0 = \left.\frac{df}{d\boldsymbol{\sigma}}\right|_{\sigma=\sigma_{trial}}$$
$$\alpha_0 = \sqrt{\frac{2}{3}\boldsymbol{n}\cdot\boldsymbol{n}}$$

4. For iteration $i = 1$ to $i_{max} = 50$

   - Update plastic strains and stresses (and h, s), and check yield functions based on n and $\Delta\lambda$ from last iteration:

     (a) Calculate the components of plastic strain for current iteration:

$$\Delta\boldsymbol{\varepsilon_{vp}} = \left[(1-T)\dot{\boldsymbol{\varepsilon}}_{\boldsymbol{vp},j-1} + T\dot{\lambda}_{i-1}\boldsymbol{n}_{i-1}\right]\Delta t$$

     where T is the interpolation parameter.

     (b) Calculate components of new stress:

$$\boldsymbol{\sigma} = \boldsymbol{\sigma}_{j-1} + \mathbb{C}[\Delta\boldsymbol{\varepsilon} - \Delta\boldsymbol{\varepsilon_{vp}}]$$

     (c) Evaluate yield function f using updated state variables:

     i. Calculate ε_p:

$$\Delta\varepsilon_p = \alpha_{i-1}\Delta\lambda_{i-1}$$
$$\varepsilon_p = \varepsilon_{p,j-1} + \Delta\varepsilon_p$$

     ii. Calculate $\dot{\varepsilon}_p$:

$$\dot{\varepsilon}_p = \alpha\dot{\lambda}$$

     iii. Calculate η, $\bar{\theta}$, $\bar{\sigma}$ (Eq. (2)), R (Eq. (9)), ε_f (Eq. (10)), D (Eq. (11)), β (Eq. (12)) and X (Eq. (19)).

     iv. Calculate the current flow stress $\sigma = \bar{\sigma}R\beta X$, and h and s (Eqs. (28) to (33)) using the updated state variables above.

     v. Evaluate $f(\boldsymbol{\sigma}, \sigma)$.

     - If $f < \mu_f$; where $\mu_f = 1\times10^{-2}$ is the tolerance on f, accept the stress update and go to step 7 (next integration point).
     - Else, use the updated stress to find new $\Delta\lambda$ and $\dot{\lambda}$ for the calculations in the next iteration:

$$\boldsymbol{n} = \frac{df}{d\boldsymbol{\sigma}}$$
$$\alpha = \sqrt{\frac{2}{3}\boldsymbol{n}\cdot\boldsymbol{n}}$$
$$\boldsymbol{P} = \left[\mathbb{C}^{-1} + T\Delta t\dot{\lambda}_{i-1}\frac{\partial\boldsymbol{n}}{\partial\boldsymbol{\sigma}}\right]^{-1}_{f} \quad \text{(Use the Sherman–Morrison [116] formula)}$$
$$\Delta\lambda = \Delta\lambda_{i-1} + \frac{}{\boldsymbol{n}\cdot\boldsymbol{P}\boldsymbol{n} + h + s/(T\Delta t)}$$
$$\dot{\lambda} = \frac{\Delta\lambda}{T\Delta t} - \frac{1-T}{T}\dot{\lambda}_{j-1}$$

     - Update $i = i + 1$ and go back to beginning of step 4.

5. If ($k > i_{max}$ and $f > \mu_f$) or otherwise nonconvergent (f =NaN), check whether last steps's D is within the tolerance $\mu_D = \max(0.05, 0.05\left(D_c - 1\right))$ from D_c. If yes, delete element.
6. Go to the next integration point and start from step 1.

Data availability

Data will be made available on request.

References

[1] BSI (British Standards Institution). BS 7910 Guide to methods for assessing the acceptability of flaws in metallic structures. BSI 2019. http://dx.doi.org/10.3403/30369478.
[2] CEN (European Committee for Standardization). prEN 1993-1-1 Draft: Eurocode 3: Design of steel structures - Part 1-1: General rules and rules for buildings. Brussels: CEN; 2020.
[3] CEN (European Committee for Standardization). prEN 1993-1-10 Draft: Eurocode 3: Design of steel structures - Part 1-10: Material toughness and through-thickness properties. Brussels: CEN; 2023.
[4] Wallin K. Low-cost J-R curve estimation based on CVN upper shelf energy. Fatigue Fract Eng Mater Struct 2001;24:537–49. http://dx.doi.org/10.1046/j.1460-2695.2001.00405.x.
[5] Feldmann M, Schaffrath S, Sandro C. Draft: background document to eurocode 3 EN 1993 – part 1-10: material toughness - approach for upper-shelf toughness requirements for the design of steel structures based on damage mechanics. Technical report, Institute of Steel Construction RWTH Aachen University; 2020.
[6] Feldmann M, Meissner M, Bartsch H, Münstermann S, Fehlemann N, Könemann M. Stand der Untersuchungen zu Werkstoffanforderungen hochfester Stähle S700 bis S960 – FOSTA-Forschungsverbund HOCHFEST. Stahlbau 2023;92:468–83. http://dx.doi.org/10.1002/stab.202300033.
[7] Feldmann M, Schaffrath S. Assessing the net section resistance and ductility requirements of en 1993-1-1 and en 1993-1-12. Steel Constr 2017;10:354–64.
[8] Eichler B, Feldmann M. Ein hochlagenorientiertes und duktilitätsgesteuertes Stahlgütewahlkonzept. Stahlbau 2016;85:25–36. http://dx.doi.org/10.1002/stab.201610349.
[9] Kuckertz C. Korrelation der Ergebnisse des Aufschweißbiegeversuchs an Stahl S355J2G3 mit Prüfverfahren nach europäischen Produktnormen. Berichte aus dem Institut für Eisenhüttenkunde, vol. 2005, 2, Aachen: RWTH; 2005.
[10] Gioielli P, Landes J, Paris P, Tada H, Loushin L. Method for predicting J-R curves from charpy impact energy. West Conshohocken, PA: ASTM; 2000, p. 61–8.
[11] Eason ED, Wright JE, Nelson EE. Multivariable modeling of pressure vessel and piping J-R data. Technical report, U.S. Nuclear Regulatory Commission; 1991.
[12] Eason ED, Nelson EE. Improved model for predicting J-R curves from charpy data. Technical report, U.S. Nuclear Regulatory Commission; 1989.
[13] Kussmaul K, Roos E. Statistical evaluation of post-yield fracture mechanics properties on the basis of the notched bar impact test. Nucl Eng Des 1985;87:123–37. http://dx.doi.org/10.1016/0029-5493(85)90101-3.
[14] Merkle JG, Johnson RE. Example calculations illustrating methods for analyzing ductile flaw stability in nuclear pressure vessels. Int J Press Vessels Pip 1985;18:35–53. http://dx.doi.org/10.1016/0308-0161(85)90025-0.
[15] Chaouadi R, Gérard R. Development of a method for extracting fracture toughness from instrumented Charpy impact tests in the ductile and transition regimes. Theor Appl Fract Mech (115):2021. http://dx.doi.org/10.1016/j.tafmec.2021.103080.
[16] Chaouadi R, Puzzolante JL. Procedure to estimate the crack resistance curve from the instrumented Charpy V–notched impact test. In: 12th international conference on fracture. 2009.
[17] Thibaux P, Müller S, Tanguy B, van den Abeele F. Ductile fracture characterization of an X70 steel: Re-interpretation of classical tests using the finite element technique. In: 2008 7th international pipeline conference, vol. 3, 2009, p. 179–86. http://dx.doi.org/10.1115/IPC2008-64291.
[18] Tanguy B, Luu TT, Perrin G, Pineau A, Besson J. Plastic and damage behaviour of a high strength X100 pipeline steel: Experiments and modelling. Int J Press Vessels Pip 2008;85:322–35. http://dx.doi.org/10.1016/j.ijpvp.2007.11.001.
[19] Xue L, Wierzbicki T. Ductile fracture initiation and propagation modeling using damage plasticity theory. Eng Fract Mech 2008;75:3276–93. http://dx.doi.org/10.1016/j.engfracmech.2007.08.012.
[20] Shinohara Y, Madi Y, Besson J. Anisotropic ductile failure of a high-strength line pipe steel. Int J Fract 2016;197:127–45. http://dx.doi.org/10.1007/s10704-015-0054-x.
[21] Zu Y, Cao Y, Zhen Y, Li F, Wu G. Determination on the fracture toughness of the welded joints of X80 pipeline steels based on small punch test. Eng Fract Mech 2023;291. http://dx.doi.org/10.1016/j.engfracmech.2023.109525.
[22] Cowper GR, Symonds PS. Strain hardening and strain-rate effects in the impact loading of cantilever beams. Technical report no. 28, Office of Naval Research; 1957.
[23] Norris DM. Computer simulation of the Charpy V-notch toughness test. Eng Fract Mech 1979;11:261–74. http://dx.doi.org/10.1016/0013-7944(79)90003-1.
[24] Wilshaw TR. Deformation and fracture of mild steel specimens. J Iron Steel Inst 1966;204.
[25] Cao TS. Models for ductile damage and fracture prediction in cold bulk metal forming processes: a review. Int J Mater Form 2015;10:139–71. http://dx.doi.org/10.1007/s12289-015-1262-7.
[26] Asserin-Lebert A, Besson J, Gourgues AF. Fracture of 6056 aluminum sheet materials: effect of specimen thickness and hardening behavior on strain localization and toughness. Mater Sci Eng: A 2005;395:186–94. http://dx.doi.org/10.1016/j.msea.2004.12.018.
[27] Rivalin F, Pineau A, Di Fant M, Besson J. Ductile tearing of pipeline-steel wide plates. Eng Fract Mech 2001;68:329–45. http://dx.doi.org/10.1016/s0013-7944(00)00107-7.
[28] Li Y, Wierzbicki T. Prediction of plane strain fracture of AHSS sheets with post-initiation softening. Int J Solids Struct 2010;47:2316–27. http://dx.doi.org/10.1016/j.ijsolstr.2010.04.028.

[29] Xue L. Damage accumulation and fracture initiation in uncracked ductile solids subject to triaxial loading. Int J Solids Struct 2007;44:5163–81. http://dx.doi.org/10.1016/j.ijsolstr.2006.12.026.
[30] Huang H, Xue L. Prediction of slant ductile fracture using damage plasticity theory. Int J Press Vessels Pip 2009;86:319–28. http://dx.doi.org/10.1016/j.ijpvp.2008.11.027.
[31] Lan W, Deng X, Sutton MA, Cheng C-S. Study of slant fracture in ductile materials. Int J Fract 2006;141:469–96. http://dx.doi.org/10.1007/s10704-006-9008-7.
[32] Novokshanov D, Döbereiner B, Sharaf M, Münstermann S, Lian J. A new model for upper shelf impact toughness assessment with a computationally efficient parameter identification algorithm. Eng Fract Mech 2015;148:281–303. http://dx.doi.org/10.1016/j.engfracmech.2015.07.069.
[33] Simha CHM, Xu S, Tyson WR. Non-local phenomenological damage-mechanics-based modeling of the drop-weight tear test. Eng Fract Mech 2014;118:66–82. http://dx.doi.org/10.1016/j.engfracmech.2014.01.009.
[34] ASTM (American Society for Testing and Materials). E436-03 (Reapproved 2021) standard test method for drop-weight tear tests of ferritic steels. West Conshohocken; 2021.
[35] ISO (International Organization for Standardization). ISO 148-1 Metallic materials - Charpy pendulum impact test - Part 1: Test method. ISO; 2016.
[36] Wong WJ, Walters CL. Effects of strain hardening and the Lode dependence of the fracture strain locus on slant fracture in Charpy V-notch impact testing. In: ASME 2024 43rd international conference on ocean, offshore and arctic engineering. ASME (the American society of mechanical engineers; 2024, http://dx.doi.org/10.1115/OMAE2024-125635.
[37] Hure J, Parrot A, Meunier S. Numerical prediction of the effect of irradiation on the Charpy upper shelf energy of reactor pressure vessel steels. J Nucl Mater 2022;570. http://dx.doi.org/10.1016/j.jnucmat.2022.153956.
[38] CEN (European Committee for Standardization). EN 10025-6 Hot rolled products of structural steels - Part 6: Technical delivery conditions for flat products of high yield strength structural steels in the quenched and tempered condition. Brussels: CEN; 2019.
[39] LR (Lloyd's Register). Rules for the manufacture, testing and certification of materials. London: LR; 2023.
[40] Wang WM, Sluys LJ, de Borst R. Viscoplasticity for instabilities due to strain softening and strain-rate softening. Internat J Numer Methods Engrg 1997;40:3839–64. http://dx.doi.org/10.1002/(sici)1097-0207(19971030)40:20<3839::Aid-nme245>3.0.Co;2-6.
[41] Johnson GR, Cook WH. Fracture characteristics of three metals subjected to various strains, strain rates, temperatures and pressures. Eng Fract Mech 1985;21:31–48. http://dx.doi.org/10.1016/0013-7944(85)90052-9.
[42] Swift HW. Plastic instability under plane stress. J Mech Phys Solids 1952;1:1–16.
[43] Considère A. Mémoire sur l'emploi du fer et de l'acier. Ann des Ponts et Chaussées 1885;9:574–775.
[44] Yun X, Gardner L. Stress–strain curves for hot-rolled steels. J Constr Steel Res 2017;133:36–46.
[45] Bannister AC, Ruiz Ocejo J, Gutierrez-Solana F. Implications of the yield stress/tensile stress ratio to the SINTAP failure assessment diagrams for homogeneous materials. Eng Fract Mech 2000;67:547–62. http://dx.doi.org/10.1016/s0013-7944(00)00073-4.
[46] ISO (International Organization for Standardization). ISO 6892-1 Metallic materials - Tensile testing - Part 1: Method of test at room temperature. Geneva: ISO; 2019.
[47] Fujii E, Ohkuma I, Kawaguchi Y, Tsukamoto M. Effects of temperature and strain rate on dynamic fracture toughness of steel. J Soc Nav Archit Jpn 1985;158:619–29.
[48] Toyosada M, Fujii E, Nohara K, Kawaguchi Y, Arimochi K, Isaka K. The effect of strain rate on critical CTOD and J. integral. J Soc Nav Archit Jpn 1987;1987:343–56. http://dx.doi.org/10.2534/jjasnaoe1968.1987.343.
[49] Itabashi M, Kawata K. Carbon content effect on high-strain-rate tensile properties for carbon steels. Int J Impact Eng 2000;24:117–31. http://dx.doi.org/10.1016/s0734-743x(99)00050-0.
[50] Choung J, Nam W, Lee J-Y. Dynamic hardening behaviors of various marine structural steels considering dependencies on strain rate and temperature. Mar Struct 2013;32:49–67. http://dx.doi.org/10.1016/j.marstruc.2013.02.001.
[51] Forni D, Chiaia B, Cadoni E. Strain rate behaviour in tension of s355 steel: Base for progressive collapse analysis. Eng Struct 2016;119:164–73. http://dx.doi.org/10.1016/j.engstruct.2016.04.013.
[52] Paik JK, Kim KJ, Lee JH, Jung BG, Kim SJ. Test database of the mechanical properties of mild, high-tensile and stainless steel and aluminium alloy associated with cold temperatures and strain rates. Ships Offshore Struct 2017;12:S230–56. http://dx.doi.org/10.1080/17445302.2016.1262729.
[53] Chen J, Shu W, Li J. Constitutive model of Q345 steel at different intermediate strain rates. Int J Steel Struct 2017;17:127–37. http://dx.doi.org/10.1007/s13296-016-0122-8.
[54] Alabi AA, Moore PL, Wrobel LC, Campbell JC, He W. Tensile behaviour of S690QL and S960QL under high strain rate. J Constr Steel Res 2018;150:570–80. http://dx.doi.org/10.1016/j.jcsr.2018.08.009.
[55] Yang X, Yang H, Zhang S. Rate-dependent constitutive models of S690 high-strength structural steel. Constr Build Mater 2019;198:597–607. http://dx.doi.org/10.1016/j.conbuildmat.2018.11.285.
[56] Yang X, Yang H, Lai Z, Zhang S. Dynamic tensile behavior of S690 high-strength structural steel at intermediate strain rates. J Constr Steel Res 2020;168. http://dx.doi.org/10.1016/j.jcsr.2020.105961.
[57] Huo J-S, Zeng X, Wang H-T. Tensile behaviour of TMCP Q690D high-strength structural steel at strain rates from 0.00025 to 760 s-1. Adv Steel Constr 2022;18:488–94. http://dx.doi.org/10.18057/IJASC.2022.18.1.7.
[58] Dong J, Elchalakani M, Li D, Xiong G, Yang B. Dynamic hardening behavior and ductile fracture of high-strength steel at intermediate strain rates. J Struct Eng 2022;148. http://dx.doi.org/10.1061/(asce)st.1943-541x.0003416.
[59] Needleman A. Material rate dependence and mesh sensitivity in localization problems. Comput Methods Appl Mech Engrg 1988;67:69–85. http://dx.doi.org/10.1016/0045-7825(88)90069-2.
[60] Bai Y, Wierzbicki T. Application of extended Mohr–Coulomb criterion to ductile fracture. Int J Fract 2010;161:1–20. http://dx.doi.org/10.1007/s10704-009-9422-8.
[61] Bai Y, Wierzbicki T. A new model of metal plasticity and fracture with pressure and Lode dependence. Int J Plast 2008;24:1071–96. http://dx.doi.org/10.1016/j.ijplas.2007.09.004.
[62] Xue L, Paredes M, Nonn A, Wierzbicki T. Modeling of crack propagation in defective X100 line pipes. In: ASME 2020 39th international conference on ocean, offshore and arctic engineering. Materials technology, vol. 3, 2020, http://dx.doi.org/10.1115/omae2020-18048.
[63] Sakonder C, Xue L, Paredes M, Savioli R, Sarzosa DFB. Directional dependence of critical axial strain in X65 pipeline steel subject to combined internal pressure and bending loading. Int J Press Vessels Pip 2022;196. http://dx.doi.org/10.1016/j.ijpvp.2022.104610.
[64] Beese AM, Luo M, Li Y, Bai Y, Wierzbicki T. Partially coupled anisotropic fracture model for aluminum sheets. Eng Fract Mech 2010;77:1128–52. http://dx.doi.org/10.1016/j.engfracmech.2010.02.024.
[65] Dunand M, Mohr D. On the predictive capabilities of the shear modified Gurson and the modified Mohr–Coulomb fracture models over a wide range of stress triaxialities and Lode angles. J Mech Phys Solids 2011;59:1374–94. http://dx.doi.org/10.1016/j.jmps.2011.04.006.
[66] Anderson TL. Fracture mechanics: fundamentals and applications. 4th ed.. Boca Raton: CRC Press; 2017, http://dx.doi.org/10.1201/9781315370293.
[67] Bao Y, Wierzbicki T. On the cut-off value of negative triaxiality for fracture. Eng Fract Mech 2005;72:1049–69. http://dx.doi.org/10.1016/j.engfracmech.2004.07.011.
[68] Tanguy B, Besson J, Piques R, Pineau A. Ductile to brittle transition of an A508 steel characterized by charpy impact test. Eng Fract Mech 2005;72:413–34. http://dx.doi.org/10.1016/j.engfracmech.2004.03.011.

[69] Seo K-W, Kim J-Y, Kim Y-J, Kim K-S. Finite element ductile fracture simulation of Charpy and drop weight tear tests for API X52. Theor Appl Fract Mech 2024;133. http://dx.doi.org/10.1016/j.tafmec.2024.104629.
[70] Taylor GI, Quinney H. The latent energy remaining in a metal after cold working. Proc R Soc Lond Ser A, Contain Pap A Math Phys Character 1933;143:307–26. http://dx.doi.org/10.1098/rspa.1934.0004.
[71] Besseling JF, van der Giessen E. Mathematical modelling of inelastic deformation. 1994.
[72] Meyers MA. Dynamic behavior of materials. John Wiley & Sons Inc.; 1994, http://dx.doi.org/10.1002/9780470172278.
[73] API (American Petroleum Institute). API 5L. Line pipe specification 5L. Washington, DC: API; 2018.
[74] Liakat M, Khonsari MM. Rapid estimation of fatigue entropy and toughness in metals. Mater Des 2014;62:149–57. http://dx.doi.org/10.1016/j.matdes.2014.04.086.
[75] Dey S, Borvik T, Hopperstad OS, Leinum JR, Langseth M. The effect of target strength on the perforation of steel plates using three different projectile nose shapes. Int J Impact Eng 2004;30:1005–38. http://dx.doi.org/10.1016/j.ijimpeng.2004.06.004.
[76] Hill R. The mathematical theory of plasticity. Oxford: Clarendon Press; 1950.
[77] DS Simulia (Dassault Systèmes Simulia). ABAQUS 2022. Commercial finite element software. 2022.
[78] de Borst R, Crisfield MA, Remmers JJC, Verhoosel CV. Nonlinear finite element analysis of solids and structures. second ed.. West Sussex, United Kingdom: John Wiley & Sons Ltd; 2012.
[79] Kuhn HW, Tucker AW. Nonlinear programming. In: Second berkeley symposium on mathematical statistics and probability. 1951, p. 481–92.
[80] Wierzbicki T, Bao Y, Lee Y-W, Bai Y. Calibration and evaluation of seven fracture models. Int J Mech Sci 2005;47:719–43. http://dx.doi.org/10.1016/j.ijmecsci.2005.03.003.
[81] Coppejans O, Walters CL. Determination of parameters for the damage mechanics approach to ductile fracture based on a single fracture mechanics test. In: ASME 2017 36th international conference on ocean, offshore and arctic engineering. OMAE; 2017, http://dx.doi.org/10.1115/OMAE2017-61425.
[82] Xin H, Veljkovic M. Evaluation of high strength steels fracture based on uniaxial stress–strain curves. Eng Fail Anal 2021;120. http://dx.doi.org/10.1016/j.engfailanal.2020.105025.
[83] Xue L, Wierzbicki T. Numerical simulation of fracture mode transition in ductile plates. Int J Solids Struct 2009;46:1423–35. http://dx.doi.org/10.1016/j.ijsolstr.2008.11.009.
[84] Morgeneyer TF, Besson J. Flat to slant ductile fracture transition: Tomography examination and simulations using shear-controlled void nucleation. Scr Mater 2011;65:1002–5. http://dx.doi.org/10.1016/j.scriptamat.2011.09.004.
[85] Besson J, McCowan CN, Drexler ES. Modeling flat to slant fracture transition using the computational cell methodology. Eng Fract Mech 2013;104:80–95. http://dx.doi.org/10.1016/j.engfracmech.2013.02.032.
[86] IACS (International Association of Classification Societies). IACS UR W requirements concerning material and welding. IACS; 2023.
[87] Ghosh AK. The influence of strain hardening and strain-rate sensitivity on sheet metal forming. J Eng Mater Technol 1977;99:264–74. http://dx.doi.org/10.1115/1.3443530.
[88] ISO (International Organization for Standardization). ISO 14556 Metallic materials - Charpy V-notch pendulum impact test - Instrumented test method. Geneva: ISO; 2023.
[89] Hosseinzadeh A, Hashemi SH, Rastegari H, Maraki MR. Investigation of the notch depth effect on Charpy fracture energy and fracture surface features of API X65 steel. Can Metall Q 2022;62:36–48. http://dx.doi.org/10.1080/00084433.2022.2066241.
[90] Nonn A, Brauer H. Establishing the correlation between charpy impact energies for different sized specimens of modern pipeline steels. In: Proceedings of the 10th international pipeline conference - 2014, vol. 3, 2014, http://dx.doi.org/10.1115/IPC2014-33164.
[91] Besson J, Luu TT, Tanguy B, Pineau A. Anisotropic plastic and damage behavior of a high strength pipeline steel. In: The nineteenth international offshore and polar engineering conference. 2009.
[92] Schmitt W, Varfolomeyev IV, Böhme W. Modelling of the Charpy test as a basis for toughness evaluation. Eur Struct Integr Soc 2002;30:45–56. http://dx.doi.org/10.1016/S1566-1369(02)80005-X.
[93] ASTM (American Society for Testing and Materials). E1820-23b Standard test method for measurement of fracture toughness. West Conshohocken: ASTM; 2023.
[94] Bakker A. Compatible compliance and stress intensity expressions for the standard three-point bend specimen. Fatigue Fract Eng Mater Struct 1990;13:145–54. http://dx.doi.org/10.1111/j.1460-2695.1990.tb00586.x.
[95] Wallin K. Rotation and bending corrections for the SE(B) specimen. Mater Perform Charact 2014;3. http://dx.doi.org/10.1520/mpc20130031.
[96] Paredes M, Wierzbicki T, Zelenak P. Prediction of crack initiation and propagation in X70 pipeline steels. Eng Fract Mech 2016;168:92–111. http://dx.doi.org/10.1016/j.engfracmech.2016.10.006.
[97] Sarzosa DFB, Paredes M, Savioli R, Ruggieri C, Leite LGTS, da Silva NS, et al. Experimental and numerical study on the ductile fracture response of X65 girth-welded joint made of Inconel 625 alloy. Theor Appl Fract Mech 2022;121. http://dx.doi.org/10.1016/j.tafmec.2022.103533.
[98] Bridgman PW. Studies in large plastic flow and fracture with special emphasis on the effects of hydrostatic pressure. New York: McGraw-Hill; 1952.
[99] Xue L. Stress based fracture envelope for damage plastic solids. Eng Fract Mech 2009;76:419–38. http://dx.doi.org/10.1016/j.engfracmech.2008.11.010.
[100] McMeeking RM. Finite deformation analysis of crack-tip opening in elastic–plastic materials and implications for fracture. J Mech Phys Solids 1977;25:357–81. http://dx.doi.org/10.1016/0022-5096(77)90003-5.
[101] Hutchinson JW. Plastic stress and strain fields at a crack tip. J Mech Phys Solids 1968;16:337–42. http://dx.doi.org/10.1016/0022-5096(68)90021-5.
[102] Rice JR, Rosengren GF. Plane strain deformation near a crack tip in a power-law hardening material. J Mech Phys Solids 1968;16:1–12. http://dx.doi.org/10.1016/0022-5096(68)90013-6.
[103] Clausing DP. Effect of plastic strain state on ductility and toughness. Int J Fract Mech 1970;6:71–85. http://dx.doi.org/10.1007/bf00183662.
[104] Benzerga AA, Besson J, Batisse R, Pineau A. Synergistic effects of plastic anisotropy and void coalescence on fracture mode in plane strain. Modelling Simul Mater Sci Eng 2002;10:73–102. http://dx.doi.org/10.1088/0965-0393/10/1/306.
[105] Xue L. Localization conditions and diffused necking for damage plastic solids. Eng Fract Mech 2010;77:1275–97. http://dx.doi.org/10.1016/j.engfracmech.2009.12.008.
[106] Banabic D, Aretz H, Paraianu L, Jurco P. Application of various FLD modelling approaches. Modelling Simul Mater Sci Eng 2005;13:759–69. http://dx.doi.org/10.1088/0965-0393/13/5/009.
[107] Li H, Fu MW, Lu J, Yang H. Ductile fracture: Experiments and computations. Int J Plast 2011;27:147–80. http://dx.doi.org/10.1016/j.ijplas.2010.04.001.
[108] Stoughton TB, Yoon JW. A new approach for failure criterion for sheet metals. Int J Plast 2011;27:440–59. http://dx.doi.org/10.1016/j.ijplas.2010.07.004.
[109] Zhu H, Zhu X. A mixed-mode fracture criterion for AHSS cracking prediction at large strain. SAE Int J Mater Manuf 2011;4:10–26. http://dx.doi.org/10.4271/2011-01-0007.
[110] Habibi N, Ramazani A, Sundararaghavan V, Prahl U. Failure predictions of DP600 steel sheets using various uncoupled fracture criteria. Eng Fract Mech 2018;190:367–81. http://dx.doi.org/10.1016/j.engfracmech.2017.12.022.
[111] Ribas LM, Gipiela ML, Lajarin SF, Filho RAC, Marcondes PVP. Comparative study of six failure criteria via numerical simulation of stamped DP600 steel. Int J Adv Manuf Technol 2022;121:2427–35. http://dx.doi.org/10.1007/s00170-022-09440-5.
[112] Pack K, Luo M, Wierzbicki T. Sandia fracture challenge: blind prediction and full calibration to enhance fracture predictability. Int J Fract 2014;186:155–75. http://dx.doi.org/10.1007/s10704-013-9923-3.

[113] Chen A, Zhang P, Chen B, Li Y, Xing J. A new ductile fracture model for Q460C high-strength structural steel under monotonic loading: Experimental and numerical investigation. Eng Fract Mech 2023;288. http://dx.doi.org/10.1016/j.engfracmech.2023.109358.
[114] Fudlailah P, Paredes M. Fracture behavior of X65 Q & T seamless pipeline steel under different strain rates and stress states. In: ASME 2020 39th international conference on ocean, offshore and arctic engineering. 2020, http://dx.doi.org/10.1115/OMAE2020-18032.
[115] Algarni M, Bai Y, Choi Y. A study of Inconel 718 dependency on stress triaxiality and Lode angle in plastic deformation and ductile fracture. Eng Fract Mech 2015;147:140–57. http://dx.doi.org/10.1016/j.engfracmech.2015.08.007.
[116] Sherman J, Morrison WJ. Adjustment of an inverse matrix corresponding to a change in one element of a given matrix. Ann Math Stat 1950;21:124–7. http://dx.doi.org/10.1214/aoms/1177729893.